Fall 12-2020

Numerical Analysis of Multi-Functional Surface Acoustic Wave Sensor

Xin Xu
Embry-Riddle Aeronautical University

NUMERICAL ANALYSIS OF MULTI-FUNCTIONAL SURFACE ACOUSTIC WAVE SENSOR

By

Xin Xu

A Thesis Submitted to the Faculty of Embry-Riddle Aeronautical University

In Partial Fulfillment of the Requirements for the Degree of

Master of Science in Aerospace Engineering

December 2020

Embry-Riddle Aeronautical University

Daytona Beach, Florida

NUMERICAL ANALYSIS OF MULTI-FUNCTIONAL SURFACE ACOUSTIC WAVE SENSOR

By

Xin Xu

This Thesis was prepared under the direction of the candidate's Thesis Committee Chair, Dr. Daewon Kim, Department of Aerospace Engineering, and has been approved by the members of the Thesis Committee. It was submitted to the Office of the Senior Vice President for Academic Affairs and Provost, and was accepted in the partial fulfillment of the requirements for the Degree of Master of Science in Aerospace Engineering.

THESIS COMMITTEE

Daewon Kim Digitally signed by Daewon Kim Date: 2020.12.03 11:51:37 -05'00'

Chairman, Dr. Daewon Kim

Member, Dr. Eduardo Rojas

Member, Dr. Mandar Kulkarni

Marwan Al-Haik Digitally signed by Marwan Al-Haik DN: cn=Marwan Al-Haik, o=Embry-Riddle Aeronautical University, ou=Aerospace Engineering, email=alhaikm@erau.edu, c=US Date: 2020.12.03 17:29:35 -05'00'

Graduate Program Coordinator, Dr. Marwan Al-Haik

Date

Dean of the College of Engineering, Dr. Maj Mirmirani

Date

Christopher Grant Digitally signed by Christopher Grant Date: 2020.12.04 10:11:11 -05'00'

Associate Provost of Academic Support, Dr. Christopher Grant

Date

ACKNOWLEDGEMENTS

My deepest gratitude goes first and foremost to Professor Daewon Kim, my supervisor, for his constant encouragement and guidance. He has walked me through all the stages of this thesis's writing and helped me get the COMSOL licenses. Without his consistent and illuminating instruction, this thesis could not have reached its present form.

Secondly, I would like to express my heartfelt appreciation to Professor Eduardo Rojas, who led me into the field of electrical engineering. I am also greatly indebted to the Professor Mandar Kulkarni to join my thesis committee and give me valuable suggestions about the numerical analysis.

Lastly, my thanks would go to my beloved family for their loving considerations, especially my girlfriend, who spent all through these two years with me and always brought me spiritual encouragement. I also owe my sincere gratitude to my friends and my fellow classmates who gave me their help and time in listening to me and helping me work out my problems during the difficult course of the thesis.

ABSTRACT

A surface acoustic wave (SAW) sensor can have broad industrial applications due to its compact size, low cost-effectiveness, and versatility of sensible measurands, as well as the wireless capabilities. In this study, a theoretical modeling approach accompanied by a MATLAB-based algorithm of the SAW device is first presented. With the designed dimensional parameters and selected material properties, numerical analyses are performed using COMSOL Multiphysics to validate the theoretical results. Various postprocessing responses of the propagated SAWs in both time and frequency domains, such as time delay, insertion loss, and frequency shift, are examined to evaluate the device performances. Also, the sensing mechanisms of multiple sensing measurands, such as mechanical strain and temperature, are investigated by scrutinizing the changes of the wave characteristics.

TABLE OF CONTENTS

ACKNOWLEDGEMENTS iii

ABSTRACT iv

LIST OF FIGURES vii

LIST OF TABLES x

NOMENCLATURE xi

1. Introduction 1
   1.1. Background 1
   1.2. Motivations and Thesis Organization 4

2. Introduction to SAW Sensor 8
   2.1. Piezoelectricity 8
      2.1.1. Piezoelectric Effect 8
      2.1.2. Mechanism and Constitutive Equations 9
      2.1.3. Piezoelectric Material and Poling Process 11
      2.1.4. Application 13
   2.2. Rayleigh Wave 13
   2.3. Principle of SAW Sensor 15
   2.4. IDT Parameter 17
   2.5. SAW Sensor Performance Parameter 19
   2.6. Summary 21

3. Theoretical Modeling of SAW Sensor 23
   3.1. Principle of COM Model 23
      3.1.1. COM First Order Differential Wave Equations 24
      3.1.2. Characteristics of Perturbation and Coupling 25
      3.1.3. COM Equations for a SAW IDT 27
      3.1.4. P-Matrix Representation of a Uniform SAW Component 29
   3.2. MATLAB Analysis Based on COM Model 30
      3.2.1. Transmission Matrix Representation 31
      3.2.2. Building Blocks and Cascading Procedures 32
   3.3. Summary 38

4. Numerical Analysis of SAW Sensor 39
   4.1. Introduction of COMSOL Multiphysics 39
   4.2. Modeling of SAW Sensor in COMSOL 40
   4.3. Time Domain Analysis 44
   4.4. Frequency Domain Analysis 47
   4.5. Comparison between the PVDF and $LiNbO_3$-based Sensors 50
   4.6. Summary 53

5. Sensing Mechanism and Calibration 54
5.1. Mechanism and Measurand 54
5.2. Strain Measurement 56
5.2.1. Model Setup 57
5.2.2. Strain Measurement Result and Discussion 60
5.3. Temperature Measurement 62
5.3.1. Model Setup 63
5.3.2. Temperature Measurement Result 65
5.3.3. Sensing Layer 66
5.3.3.1 Thickness of the Sensing Layer 69
5.3.3.2 Thermal Expansion Coefficient of the Sensing Layer 69
5.4. Summary 70

6. Conclusion and Recommendation 72
6.1. Conclusion 72
6.2. Recommendation 72

REFERENCES 74

APPENDIX A – MATLAB Algorithm 78

APPENDIX B – Principles of the COMSOL Analysis 81

APPENDIX C – A Validation of COMSOL with the Published Work 85

LIST OF FIGURES

Figure		Page
2.1	Schematics of direct and converse piezoelectric effects	8
2.2	Electric dipole alignment a) before, b) during, and c) after the poling process	12
2.3	Schematic of the Rayleigh wave propagating in an elliptical motion (Jones, 2010)	14
2.4	Two configurations of the SAW sensor: a) delay line and b) two-port resonator	15
2.5	Schematic of a two-port SAW-DL sensor	16
2.6	Patterns of a) single-electrode and b) double-electrode IDTs	18
2.7	Diagram of the S-parameters in a two-port transmission line system	19
3.1	The top and side views of the SAWs propagating through the reflector gratings	24
3.2	Wave attenuation along the propagating directions	25
3.3	Schematic of a single-finger IDT model with three ports	27
3.4	Boundary conditions of a uniform SAW IDT	28
3.5	A three-port transmission line with two acoustic fields and one electrical field	31
3.6	Building blocks of a SAW transmission system	32
3.7	Building blocks of a finger pair cascaded	33
3.8	The transmission line of a three-component SAW device	36
3.9	A two-port SAW device with two characteristic impedance	37
4.1	A COMSOL SAW-DL sensor geometry with a poling direction along the z-axis	41
4.2	Boundary conditions of the SAW sensor model in a transparent view	43

Figure Page

4.3 Meshed condition of the SAW sensor model..... 44

4.4 A 2.5 MHz impulse sinusoidal signal lasting 7.2 μs (partially presented in the plot from t=0 to 2 μs)..... 45

4.5 Leading and cross-section views of the SAW sensor at the time of a), c) t=4 μs and b), d) t= 6.8 μs..... 46

4.6 Signal response from the transient analysis..... 47

4.7 Terminal setting with a 0.01 W input power and 50 Ω characterized impedance..... 48

4.8 S11 and S21 responses evaluated by a) COMSOL and b) MATLAB..... 49

4.9 Signal response of the LiNbO3-based sensor from the transient analysis..... 51

4.10 S11 and S21 responses of a LiNbO3-based SAW sensor..... 52

5.1 Example of a calibration diagram with a linear trendline..... 56

5.2 Schematic of a cuboid Al base setup with the left boundary fixed..... 57

5.3 Strain distributions of the model setup under a strain level of 0.005 along the direction a) parallel and b) perpendicular to the x-axis..... 59

5.4 Frequency shifts of a) parallel and b) perpendicular cases..... 61

5.5 Calibration diagrams of both parallel and perpendicular cases supplemented with linear trendlines..... 62

5.6 Von Mises stress distribution of the model setup under the temperature level of 350 *K*..... 64

5.7 Frequency shifts of the SAW temperature sensor under linear levels of temperature conditions with an incremental step of 30 *K* and an intact (reference) temperature of 293.15 *K*..... 65

5.8 Calibration diagram of the SAW temperature sensor with a linear trendline..... 65

5.9 Schematic of a sensing layer coated on a two-port SAW-DL sensor..... 66

5.10 Frequency shifts of the SAW temperature sensor with a 3.6×3.5×0.02 *mm* sensing layer..... 68

Figure Page

5.11 Comparison of sensitivities between the SAW sensors without (orange) and with (blue) a sensing layer..... 68

5.12 The effects of the thickness of a sensing layer on sensor sensitivity..... 69

5.13 The effects of the thermal expansion coefficient of a sensing layer on sensor sensitivity..... 70

B.1 Feature tree of a piezoelectric-thermal-combined analysis environment..... 81

C.1 Frequency response of delay line obtained from (Krishnamurthy, 2007)..... 85

LIST OF TABLES

Table		Page
4.1	Dimensional parameters of the designed SAW sensor.....	41
4.2	Material properties of the PVDF-based SAW sensor (Comsol, 2007).....	42
4.3	Material properties of the LiNbO3 substrate (Comsol, 2007).....	50
4.4	A comparison of the information obtained from the two signal responses using PVDF and LiNbO3 as substrate.....	51
5.1	Thermal properties of the LiNbO3-based SAW sensor (Comsol, 2007).....	63
5.2	Elastic and thermal properties of the Polyethylene sensing layer (Comsol, 2007).....	67
C.1	Velocity and reflectivity calculated by (Kannan, 2006).....	86

NOMENCLATURE

SAW	Surface acoustic wave
SHM	Structure health monitoring
NDE	Non-destructive evaluation
IDT	Interdigital transducer
COM	Coupling of modes
FEA	Finite element analysis
OFC	Orthogonal frequency coding
PVDF	Polyvinylidene fluoride
$LiNbO_3$	Lithium niobate
P-wave	Longitudinal (pressure) wave
S-wave	Transverse (shear) wave
SAW-DL	Surface acoustic wave-delay line
SAWR	Surface acoustic wave resonator
S-parameter	Scattering parameter
Z-parameter	Impedance parameter
Y-parameter	Admittance parameter
IL	Insertion loss
Q-factor	Quality factor
DUT	Device under test
SPUDT	Single-phase unidirectional transducer
BC	Boundary condition
PDE	Partial differential equation

MEMS	Microelectromechanical system
VNA	Vector network analyzer
ppm	Parts per million
RMS	Root mean square
DOF	Degree of freedom
T_c	Curie temperature
T_p	Mechanical stress
S_q	Mechanical strain
D_i	Electric displacement
E_k	Electric field
c_{pq}^E	Elastic stiffness constants
e_{kp}	Piezoelectric stress constants
ε_{ik}^S	Dielectric (permittivity) constants
s_{pq}^E	Elastic compliance constants
d_{iq}	Piezoelectric strain constants
k^2	Electromechanical coupling factor
v_R	Rayleigh wave velocity
v_S	Shear wave velocity
G	Shear modulus
ρ	Density
p	Period length of IDT
λ	Wavelength
f_0	Center frequency

η	Metallized ratio
S_{11}	11 element of a 2-port scattering matrix
S_{21}	21 element of a 2-port scattering matrix
Δf	3 dB bandwidth
Q	Quality factor value
N_p	Numbers of finger pair
ω	Angular frequency
$R(x,\omega)$ & $S(x,\omega)$	Counter-propagating scaler waves in COM model
$k_R(x,\omega)$	Rayleigh wavenumber
$\alpha(x,\omega)$	Attenuation parameter
$\gamma(x,\omega)$	Reflection parameter
$\xi(x,\omega)$	Transduction parameter
$\delta(x,\omega)$	Detuning parameter
$\xi(x,\omega)$	Transduction parameter
$\psi(x,\omega)$	Parameter dependent on the electrode resistance and capacitance, and the dimensions of the IDT
d	Delay line distance
Z_i	Complex characteristic impedance
R_i	Real part of the complex characteristic impedance
υ	Poisson's ratio
E	Young's modulus
f_s	Dimensionless fractional frequency shift
S_{SAW}	Relative sensitivity of SAW sensor

α	Thermal expansion coefficient
k	Thermal conductivity
C_p	Heat capacity

1. Introduction

In this chapter, a literature review for the developments of the SAW devices, especially the SAW sensor, is presented with their various types, applications, modeling approaches and research work. The thesis objectives are described along with the motivations and improvements in addition to the existing publications. Finally, an overall thesis organization is presented to provide an overview of the thesis work.

1.1. Background

The surface acoustic wave (SAW) device gathers many hot topics in a wide range of daily life, such as communications, medical equipment, and structural health monitoring (SHM). It has extensive and versatile applications, e.g., SAW filters, oscillators, identifications, and sensors, in which, the SAW sensor is the main object for the thesis study. This section briefly introduces the roadmap of the SAW devices and SAW sensors, as well as some of the publications related to the specific research directions of the SAW sensors, on which the thesis concentrates.

The theory of surface acoustic waves was first raised by (Rayleigh, 1885) with some mathematical descriptions and predictions of their properties. In the 1960s, people became more interested in the surface acoustic wave and believed the SAW devices could be useful for radar and non-destructive evaluation (NDE) equipment. Some theoretical publications demonstrated the ideas of “transducers” to generate the surface acoustic wave (Crabb, Maines, & Ogg, 1971; Hartemann & Dieulesaint, 1969; Kharusi & Farnell, 1970). Later on, the first SAW device was fabricated by (White & Voltmer, 1965). They designed a uniform interdigital transducer (IDT) attached to a crystal quartz substrate, the combination of which was able to piezoelectrically generate a plane SAW

propagating along a certain direction. The studies about the SAW device were developed rapidly right after them. Both of the designs of IDTs and the piezoelectric materials' selections for the substrates were under higher requirements (Diaz, Karrer, Kusters, Matsinger, & Schulz, 1975; Sittig & Coquin, 1968; Smith & Pedler, 1975), along with whom, the photolithography technology was developed for IDT fabrication. It was also found that the performance of the SAW device is the frequency and IDT dimensional-dependent. The SAW device today can have millions of productions every day for a wide range of applications.

In the recent sensing field, the SAW sensor appears to be a preferred choice comparing to the conventional sensors and is in great demand. It has a compact size, low cost, high sensitivity, and good flexibility. It can detect and measure multiple measurands such as mechanical strain and pressure, chemical and medical parameters, humidity, gas, and temperature. Most importantly, its wireless and passive capabilities exactly meet the requirements to work in harsh environments and inaccessible locations without the need for a battery. The inspirations for the SAW sensor started in the 1980s when people found that the physical and chemical phenomena mentioned above could affect the properties and characteristics of SAW devices. The studies about the SAW sensor can be classified as the designing part, modeling, simulation and optimization part, fabrication and experimental testing part, and sensing mechanism and calibration part. This thesis pays the main attention to the theoretical and numerical analyses, as well as the sensing mechanism and calibration parts.

With the fast improvements of the SAW technologies, several analytical approaches and experimental achievements are published for different sensing cases. From the 1960s,

studies about analytical methods to predict the SAW device performance in terms of some device parameters were springing up. (Smith, Gerard, Collins, Reeder, & Shaw, 1969) came up with the equivalent circuit model, which was a one-dimension model that took advantage of admittance matrices to relate the terminals. Then, a delta function model was developed by (Tancrell & Holland, 1971). It was discussed that various transfer functions of different transducer types could be derived to obtain an overall device response. This method was intuitive and convenient, whereas lacking the consideration of electrical effects such as device impedance and circuit factors. After that, (Hartmann, Bell, & Rosenfeld, 1973) combined the advantages of both methods and developed an approach called the impulse response model.

For recent studies, people sought to have high accuracy approaches instead of conventional methods. In 1979, a 3 by 3 P-matrix model describing the relations between the SAW and electric field in terms of the variables from electrical and mechanical properties was developed (Tobolka, 1979). In 1989, the coupling of modes (COM) model, which was initially used for microwave studies, was well applied to the SAW device by (Wright, 1989). It was presented by a set of COM differential wave equations and able to derive all the elements of P-matrix. The COM model is the most popular modeling approach for the SAW device at present. Based on the COM model, many further developments were done, in which a transmission matrix approach (Ro, Tung, & Wu, 2004) turned the P-matrix to a transmission matrix, thus making the cascading of SAW device components more convenient. The use of the combined COM model and transmission matrix is emphatically introduced in the later chapter.

When it came to the late 20th century, the finite element analysis (FEA) tools were used for solving the complex device geometry and material properties with precise results as the fast evolutions of the computer industry. There have been many publications that used different FEA software, e.g., CoventorWare, ANSYS, COMSOL to simulate the SAW sensor, and evaluate the device responses through different parameters such as insertion loss, eigenfrequency, and time delay (Achour, Aloui, Fourati, Zerrouki, & Yaakoubi, 2018; El Gowini & Moussa, 2009; Elsherbini, Elkordy, & Gomaa, 2016; Krishnamurthy, 2007).

Besides the analytical methods, a large number of SAW sensors have been designed and manufactured for industries, researches, and commercial applications. A team of the University of Central Florida (UCF) worked on a project with NASA to design and fabricate wireless SAW sensors use orthogonal frequency coding (OFC) and passive RFID techniques (Humphries et al., 2016; Malocha, Puccio, & Gallagher, 2004). This OFC coding technique well solved the difficulties for the data acquisition of a multi-sensor sensing environment. Similarly, various wireless SAW sensors have been used to sense mechanical strain (Donohoe, Geraghty, & O'Donnell, 2010), pressure (Binder, Bruckner, Schobernig, & Schmitt, 2013), torque (Ji et al., 2014), gas (Devkota, Ohodnicki, & Greve, 2017), temperature (Reindl, Shrena, Kenshil, & Peter, 2003) and biological indices (Länge, Rapp, & Rapp, 2008).

1.2. Motivations and Thesis Organization

Firstly, in aerospace structures, tragic failures due to various types of damage such as crack, fatigue, and creep should be avoided. People are looking for advanced monitoring systems with versatile sensors to achieve the sensing of a wide range of measurands.

There have been a lot of SHM sensors developed for different target measurands. However, they may either possess only single functionality (e.g., the strain gauge can only measure the strain, the thermal couple can only sense the temperature) or not have the wireless and passive capabilities like the fiber optics, which are easily limited by the complex and heavy wired setup. A SAW sensor can exactly deal with these two drawbacks, and its multi-functionality is studied as one of the objectives of the thesis work.

Secondly, the general constructions of a SAW sensor testing environment are always complicated, costly, and time-consuming. The innovations of commercial software for structural numerical analysis make it possible to accurately simulate the actual phenomena without conducting real operations. The analyses about the mechanisms and calibrations of the SAW sensor for real-life applications are involved with many factors and difficulties such as 1) multiple sensing cases, e.g., mechanical strain, pressure, and temperature; 2) different constitutions and material selections in order to fit corresponding sensing cases; 3) difficult background setups to achieve the desired levels of sensing measurands; in which, plenty of repetitive and unnecessary works may occur. These can be avoided if the correct study directions and efficient operation steps are figured out at the first stage of the research, which are analyzed by COMSOL Multiphysics in this study.

A few limitations by the previous publications are concluded, and some new achievements are made in the thesis work. Firstly, most publications about the numerical analysis of a SAW sensor mainly focused on evaluating a partial geometry (either 2D or reduced 3D) or coarse meshed size for saving computational time. To exhibit a closer-to-

life performance with more reliable results, an integrated geometry that considers all the components of a SAW sensor and the exact boundary conditions is analyzed. Secondly, although many SAW sensors have been developed, there are no systematic analyses about the multi-functional sensing ability of a designed SAW sensor. The thesis aims to demonstrate that a basic SAW sensor can achieve the measurements of multiple factors with corresponding factor-sensitive layers (sensing layers). Moreover, the numerical analysis has not been widely used for finding the SAW sensor mechanisms. The thesis intends to explore the ability of numerical analysis tool for establishing the calibrations of the designed SAW sensor between the measurands and device response information.

Chapter 2 starts to bring out the details of the SAW devices. The piezoelectricity mechanisms are presented, including the piezoelectric effect and constitutive equations, piezoelectric material types and poling process, and applications. Some essential properties of the Rayleigh wave that the SAW device is based on are also shown. The principle of the SAW device is then mainly introduced, and the parameters that are related to the device characteristics for design, optimization and data processing are exhibited.

Chapter 3 concentrates on the theoretical modeling using the coupling of modes (COM) theory complemented with MATLAB algorithm. The derivation of COM solutions is shown in detailed steps, and a transmission matrix approach is developed based on the COM solutions to perform the cascading response of the overall device in the MATLAB algorithm. The theoretical modeling aims to verify the device responses evaluated from the numerical analysis shown in the following chapter.

Chapter 4 implements the numerical analysis of the designed SAW sensor using COMSOL Multiphysics. Meaningful responses such as a signal response from the time domain and the insertion loss from the frequency domain are evaluated to figure out the sensor performance. Using the constants provided in the chapter, the MATLAB algorithm is run with solutions to validate the numerical analysis. At the end of the chapter, a comparison between the Polyvinylidene fluoride (PVDF) and Lithium Niobate ($LiNbO_3$) as the SAW substrate materials are discussed.

Chapter 5 explores the sensing mechanisms of the designed SAW sensor for different measurands to demonstrate its multi-function sensing ability. The strain and temperature are the two typical phenomena within the mechanical and thermal domains, which are chosen as the measurands for implementing the numerical analysis in this chapter. The SAW sensor is calibrated by establishing the functional relation between the variations of device response and the measurand level. Some factors that may influence the sensing effects are discussed.

Chapter 6 makes the conclusions for the whole thesis study. Both theoretical and numerical analyses present desired solutions and are well-matched by each other. The results from strain and temperature measurements are acceptable with some principles of a sensing layer summarized. Several recommendations for future work are also listed.

2. Introduction to SAW Sensor

In this chapter, a deeper introduction of the SAW device, especially the SAW sensor, is presented with the fundamental knowledge of piezoelectric materials and Rayleigh wave properties, the principles of SAW devices, and a set of device parameters involved with the design, optimization, and data postprocessing.

2.1. Piezoelectricity

2.1.1. Piezoelectric Effect

The piezoelectric effect refers to the phenomenon that the electric charge and mechanical strain of a material can be transformed from one to another. Due to this reversible electromechanical interaction, the piezoelectric effect can be classified as the direct effect (voltage generated by external stress) and the converse effect (strain generated by applied electric potential), as shown in Figure 2.1.

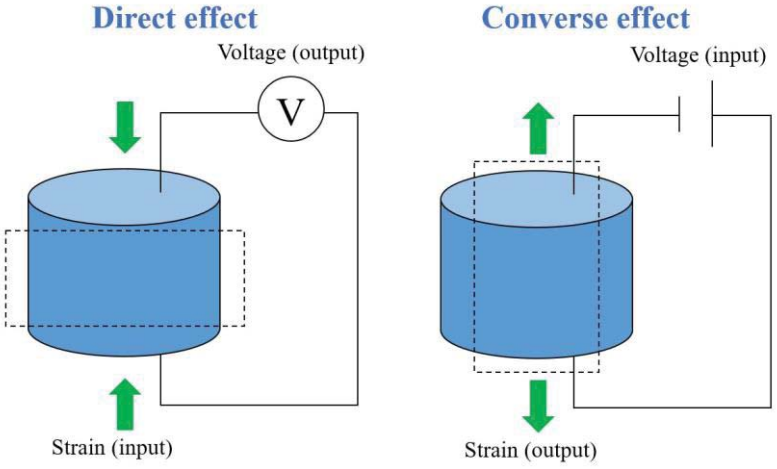

Figure 2.1 Schematics of direct and converse piezoelectric effects.

The studies about piezoelectricity can date back to the 18th century when Curie's brother found the direct piezoelectric effect in some specific materials, such as quartz and

topaz. The Curie temperature T_c (Hu, 2011) is named after them, above which, the piezoelectric material loses its ability to polarize spontaneously. Generally, the piezoelectric materials are not allowed to work beyond the temperature of $0.5T_c$. Thus, the piezoelectric structure under potential high temperature working conditions has higher requirements for material selections.

2.1.2. Mechanism and Constitutive Equations

The basic principle underlying the piezoelectricity is the shift of positive and negative electrical charges caused by the external loads. The piezoelectric materials do not have the symmetrically arranged molecular units but keep the overall electrical charge balanced. For the direct piezoelectric effect, once it undergoes external mechanical stress, the units move due to the body's deformation, disrupting the overall charge balance. Eventually, a voltage occurs on the structure. Conversely, by applying an electrical potential on the body, both the positive and negative charges align with the specific directions that contribute to the structure's deformation.

To better describe the electromechanical coupling in a visualized and quantitative form, a couple of piezoelectric constitutive equations (Meitzler et al., 1988) for the direct effect are developed as:

$$T_p = c_{pq}^E S_q - e_{pk} E_k \tag{2.1}$$

$$D_i = e_{iq} S_q + \varepsilon_{ik}^S E_k \tag{2.2}$$

where i, k=1, 2, 3; p, q=1, 2, 3, 4, 5, 6. T_p (Pa) and S_q (dimensionless) denote the mechanical stress and strain components for the mechanical domain, and D_i (Coulomb/m^2) and E_k (Volt/m) represent the electric displacement and field components

for the electric domain. c_{pq}^{E} (Pa), e_{kp} (Coulomb/m^2) and ε_{ik}^{S} (dimensionless) stand for the 21 independent elastic stiffness, 18 independent piezoelectric stress, and 6 independent dielectric (permittivity) constants in general, respectively. The superscript *E* of the c_{pq}^{E} means that the elastic stiffness constants are measured when the electric field $E_k=0$, and the same rule as ε_{ik}^{S}. These 3 coefficients are used to relate the 4 couplings between the 4 components.

Equations 2.1-2.2 are the stress-charge form of the piezoelectric constitutive equations. A strain-charge form can also be developed as:

$$S_p = s_{pq}^{E} T_q + d_{pk} E_k \tag{2.3}$$

$$D_i = d_{iq} T_q + \varepsilon_{ik}^{S} E_k \tag{2.4}$$

where s_{pq}^{E} (Pa^{-1}) and d_{iq} (m/Volt or Coulomb/N) are the elastic compliance and piezoelectric strain constants. They follow the relations of:

$$c_{pr}^{E} s_{rq}^{E} = \delta_{pq} \tag{2.5}$$

$$e_{ip} = d_{iq} c_{qp}^{E} \tag{2.6}$$

where r=1, 2, 3, 4, 5, 6, and δ_{pq} is the unit matrix. e_{ip} and d_{iq} are two different forms of piezoelectric constants, which may be useful for analyzing the different cases. The electromechanical coupling factor, k^2, is defined as the ratio of stored electrical energy to input mechanical energy for the direct piezoelectric effect (Uchino, 2017), vice versa. It reflects the conversion rate between the two energy domains, which can be expressed by the known material properties as:

$$k_{ij}{}^2 = \frac{d_{ij}{}^2}{\varepsilon_{ii}^S s_{jj}^E} \tag{2.7}$$

The electromechanical coupling factor is an essential parameter showing the intensity of piezoelectricity for a material, which should be taken into account for a piezoelectric-based structure, as well as other parameters, e.g., energy transmission coefficient, mechanical quality factor.

2.1.3. Piezoelectric Material and Poling Process

Piezoelectric materials are the materials that have the ability to perform the piezoelectric effect under the applied mechanical or electrical loads spontaneously or after an artificial poling process. These materials can be classified as single crystals, ceramics, polymers, and composites.

Normally, most potential piezoelectric materials do not exhibit polarization with all the microscopic electric dipoles aligned towards one certain direction. Instead, their dipoles are initially randomly oriented, as shown in Figure 2.2(a), which causes the materials not sensitive enough to perform the piezoelectric effect. Therefore, a poling process is required to enforce the dipoles' alignment for better piezoelectricity.

The poling process is done by applying a very high electric field along the desired direction onto the material. During the poling, each dipole is subjected to a torque, which turns it parallel to the electric field. All the dipoles are strictly well oriented after a short period of poling, as shown in Figure 2.2(b). Once the electric field is switched off, the dipoles do not maintain the exact same direction, whereas they are roughly aligned, as shown in Figure 2.2(c). This alignment is permanent and completely re-orientable by doing the same process. The ability to generate the polarization when sustaining an

electric field and keep this polarization after removing the electric field is called ferroelectricity, a subset of piezoelectricity.

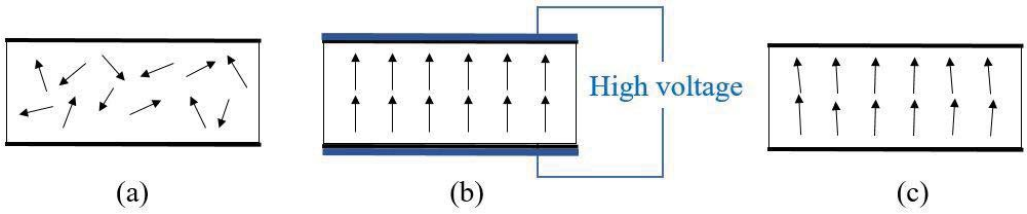

Figure 2.2 Electric dipole alignment a) before, b) during, and c) after the poling process.

The piezoelectric ceramics comprise masses of microscopic grains that are in the form of a perovskite crystal cell. This structure type gives the material a high electromechanical coupling factor and elastic stiffness, but a low thermal expansion coefficient, conductivity, and makes the material more brittle. The most popular piezoelectric ceramics nowadays are the lead zirconate titanate (PZT) and barium titanate ($BaTiO_3$).

The piezoelectric polymers take advantage of their long polymer chains that provide the material sufficient flexibility to shape and perform mechanical strain, stress, and moment. However, the polymers that have a low electromechanical coupling factor and elastic stiffness are usually more expensive than the ceramics. Polyvinylidene fluoride (PVDF) is known as the most preferred piezoelectric polymer.

In addition, some single crystals, such as Lithium niobate ($LiNbO_3$) and quartz (SiO_2), also perform piezoelectricity. They are found to have higher electromechanical properties than their crystalline counterparts, and are thus of great interest to researchers (Akdogan, Allahverdi, & Safari, 2005). However, they are still faced with the difficulties in homogeneous deposition and reproduction.

The piezoelectric composites that are integrated by the micro and nano-fillers are able to fix the challenges of the above material types and possess only the advantages of them; hence they are involved in high demands for piezoelectric industries.

2.1.4. Application

Piezoelectricity has numerous applications in the industrial fields. The direct piezoelectric effect can be used as 1) high-voltage power sources, e.g., ignitors and lighters; 2) mechanical sensors such as strain sensor, pressure sensor, and 3) energy harvestings that store the electrical energy from the external mechanical energy. Meanwhile, the converse piezoelectric effect can be used in multiple areas, which are 1) industrial applications such as motors, stack actuators; 2) medical devices like ultrasonic equipment and 3) consumer electronics, e.g., speakers, buzzers, inkjet printers, toothbrushes.

The SAW device is the main object of the thesis that works as a transducer taking advantage of both direct and converse piezoelectric effects. The detailed research about the SAW device, especially the SAW sensor, is presented in the latter sections and chapters.

2.2. Rayleigh Wave

Rayleigh wave, one type of the surface waves, is the wave mode that the SAW device bases on, as shown in Figure 2.3. The concept of the Rayleigh wave was first raised by (Rayleigh, 1885). It exists near the free surface of a solid and performs an in-plane elliptical motion with its normal perpendicular to the propagation direction (Haldar, 2018). The amplitude of the Rayleigh wave attenuates along the thickness direction of the

solid and only keeps within a specific depth. The depth varies for different materials but is approximately equal to one wavelength.

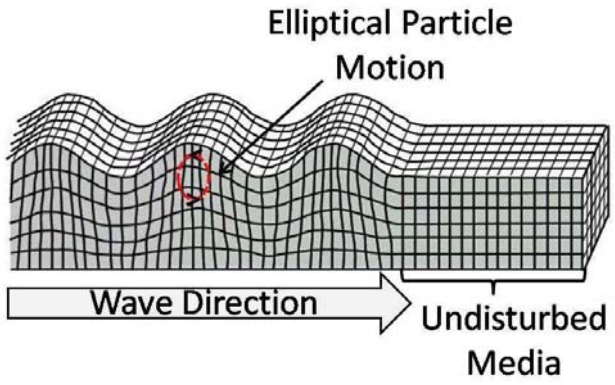

Figure 2.3 Schematic of the Rayleigh wave propagating in an elliptical motion (Jones, 2010).

Rayleigh waves travel slower than the longitudinal wave (P-wave) and transverse wave (S-wave). The velocity of the Rayleigh wave is a crucial factor for the device response characteristics and is initially determined by the material properties, which is roughly computable. For a homogeneous material, the Rayleigh wave velocity is affected by its elastic moduli and density. A formula that approximates the Rayleigh wave velocity v_R is given as (Freund, 1998):

$$v_R = v_S \frac{0.862 + 1.14\nu}{1 + \nu} \tag{2.8}$$

where υ is the Poisson's ratio, and v_S denotes the shear wave velocity that can be expressed by the shear modulus G and density ρ:

$$v_S = \sqrt{\frac{G}{\rho}} \tag{2.9}$$

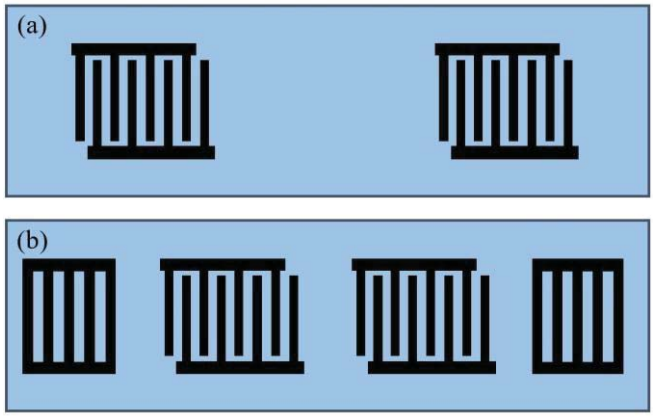

Figure 2.4 Two configurations of the SAW sensor: a) delay line and b) two-port resonator.

2.3. Principle of SAW Sensor

SAW sensor has a broad range of applications, which are generally classified as the SAW delay line (SAW-DL) and resonator (SAWR) by its functionalities (Figure 2.4). As its name implies, the SAW-DL separates the transducers by a certain length of the delay line to transmit the wave signal. Therefore, it is usually a two-port device. The SAW-DL doesn't gather certain resonator frequencies; thus, its working principle is to capture the phase variations of the frequency response (Hohmann et al., 2015). By delaying the signal, the target analyte can be adequately measured through these variations. The SAWR has the same configuration of the transducer with SAW-DL, but additional reflective gratings put at both left and right sides of the transducer, which can be either a one or two-port device. With the help of the gratings, the frequencies near the resonate frequency are superimposed in the frequency response, which produces cavity resonant. The thesis mainly focuses on the analyses of a two-port SAW-DL sensor.

A two-port SAW-DL sensor mainly consists of a piezoelectric substrate (sometimes also a thin piezoelectric film bonded on a non-conductive substrate), a transmitting (input), and receiving (output) interdigital transducers (IDTs), and a delay line region, as

shown in Figure 2.5. When a SAW sensor works, an RF signal first excites the input IDT. Due to the converse piezoelectric effect, the IDT converts electrical energy into mechanical energy, which generates a periodic strain under each electrode and forms the elastic Rayleigh wave on the substrate. The wave propagates through the substrate surface and is converted back to the electrical signal at the output IDT. Important information from the device responses can be extracted in both time and frequency domains with different sensing mechanisms.

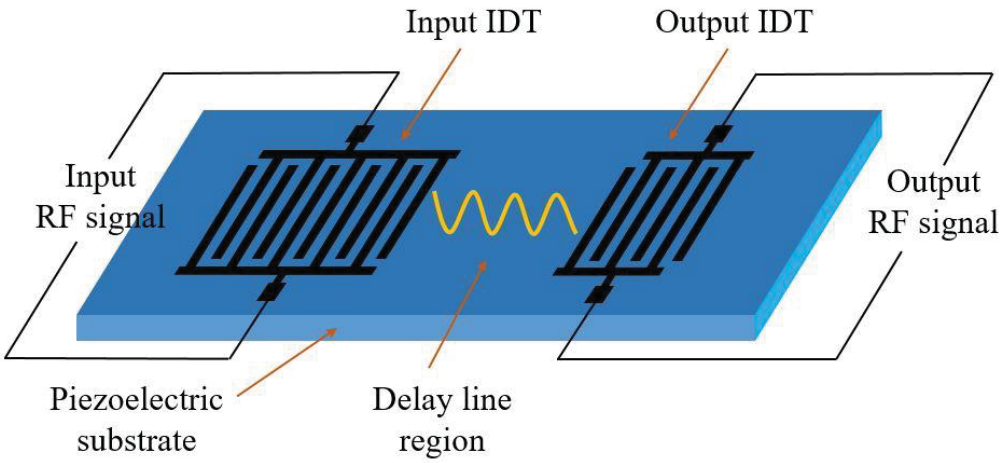

Figure 2.5 Schematic of a two-port SAW-DL sensor.

When the SAW sensor is exposed to a targeted sensing measurand, such as the mechanical strain, torque, and pressure, a variation in the properties of the propagating waves occurs, where these changes of SAW characteristics can be captured by the SAW sensor and presented through the device response and further data postprocessing. In order to achieve the sensing ability, a calibration that functionally correlates the level of ambient measurand with the changes of device responses is required. These changes can

be a shift in the center frequency and time delay, and a change of the magnitude of frequency response.

Unlike sensing the mechanical phenomena, the SAW sensor is generally not sensitive enough to most factors such as gas, humidity, temperature, and chemicals/bio-chemicals. Therefore, a functional sensing layer may be needed for the SAW sensor, which is usually coated on the delay line region. A certain sensing layer can provide sufficient selectivity for a particular type of measurand that can increase the sensor's sensitivity. The impacts from the measurand are easily caught and absorbed by the sensing layer, which are transduced to the changes of SAW characteristics.

2.4. IDT Parameter

The interdigital transducer (IDT) is often used to generate the periodic SAWs under the piezoelectric effect and convert it back to the electrical signals. An IDT basically consists of a series of metal strips regularly aligned and alternately connected to a couple of busbars.

As known, quite a few parameters such as center frequency, bandwidth, and electric impedance of a SAW device are highly dependent on the dimensions of its IDT. It's essential to have a good design and optimization for the IDT dimensions. Generally, the period length p of an IDT is equal to the wavelength λ of the generated SAW, which is decided by both center frequency f_0 and SAW velocity v_R as:

$$p = \lambda = \frac{v_R}{f_0} \tag{2.10}$$

Figure 2.6 (a) shows the schematic of a single-electrode (single-finger) IDT type with its period length p=2×(a+b), where a and b denote the widths of the finger and free space,

respectively. For a widely used metallized ratio $\eta=a/(a+b)=0.5$, the finger width can be seen as a quarter wavelength. The single-finger IDT is widely used because its wider finger width compared to the double-finger IDT can reduce the requirements for the fabrication technique.

The double-finger-type (split) IDT doubles the finger adjacently, shown in Figure 2.6 (b), with a finger width equal to $\lambda/8$ with a metallized ratio $\eta=0.5$. This IDT type reduces the reflection interference because its Bragg frequency reaches twice its center frequency (Chen & Haus, 1985). Therefore, the double finger IDT is preferably used when a precise device response is required.

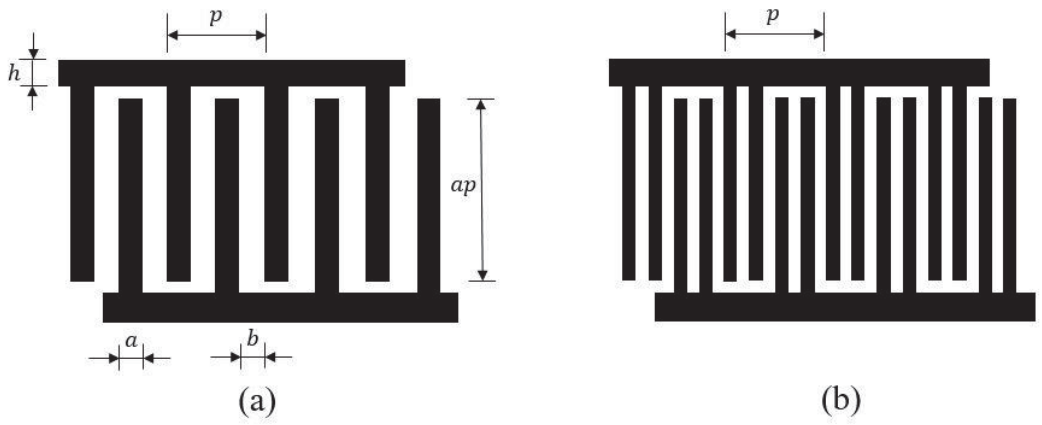

Figure 2.6 Patterns of a) single-electrode and b) double-electrode IDTs.

The electrical impedance of the SAW device needs to be taken into great consideration, in which an impedance mismatch in a network can contribute to the unnecessary signal loss (Rathod, 2019). The electrical impedance is generally related to several factors such as the material properties of the substrate (e.g., electromechanical coupling factor k^2, permittivity ε), the dimensions of IDT (e.g., acoustic aperture ap, metallized ratio η, numbers of finger pair N_p and height of busbar h). The finger thickness

t also matters with the device performance. A thinner IDT causes a larger electric resistance, while a thicker IDT puts more mass loading onto the substrate that affects the device response.

2.5. SAW Sensor Performance Parameter

The performance of a SAW device can be evaluated through multiple parameters in different aspects such as scattering parameters (S-parameter) and admittance parameters (Y-parameters), insertion loss (*IL*), and quality factor (Q-factor).

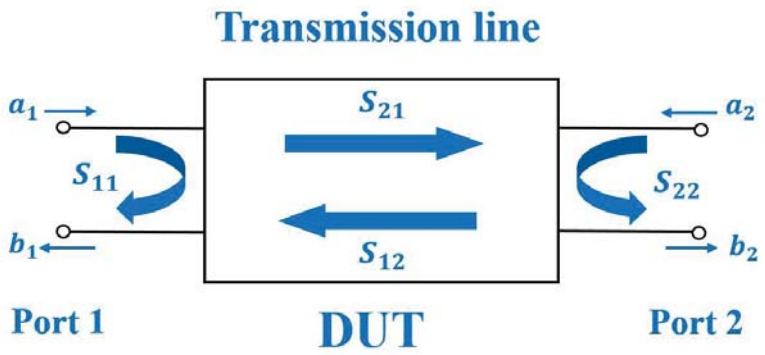

Figure 2.7 Diagram of the S-parameters in a two-port transmission line system.

The S-parameters are the elements of a frequency-dependent matrix that model the reflection and transmission characteristics of a defined transmission line system (Soluch, 2000). An n-dimensional scattering matrix can be used to describe an n-port network. Figure 2.7 shows the schematic of the four S-parameters of a device under test (DUT) in a two-port transmission line system. The first digit of the subscript represents the port number where the signal is imported, and the second digit is the port number where the signal is coming out.

Therefore, the S_{11} and S_{22} exhibit the reflection characteristics of the forward and backward measurements, meanwhile, the S_{21} and S_{12} show the transmission

characteristics of the transmission line. A matrix form transmission equation can be developed as:

$$\begin{bmatrix} a_1 \\ b_1 \end{bmatrix} = \begin{bmatrix} S_{11} & S_{12} \\ S_{21} & S_{22} \end{bmatrix} \begin{bmatrix} a_2 \\ b_2 \end{bmatrix} \tag{2.11}$$

where a_i and b_i (i=1, 2) represents the incident and reflected signal of each port.

The insertion loss (*IL*) denotes the loss of power due to the insertion of a component when the signal travels through a transmission system, which is usually expressed in decibel (Augustine et al., 2016). There are three main reasons causing the insertion loss, which are the reflected loss, dielectric loss, and copper loss. The *IL* presents the transmitting ability of a network and is often used to plot the device frequency response, which can be defined by the S_{21} parameter in decibel form, as well as the decibel ratio of the power out (P_{out}) and in (P_{in}) of the network:

$$IL = -20\log_{10}|S_{21}| \; dB = -10\log_{10}\frac{P_{out}}{P_{in}} \tag{2.12}$$

The quality factor (Q-factor) is a dimensionless parameter that refers to the damping level of a resonator, and it also describes the relationship between the center frequency (f_0) and bandwidth of a resonator as (Bell & Li, 1976):

$$Q = \frac{f_0}{\Delta f} \tag{2.13}$$

where Δf is the 3 *dB* bandwidth.

A higher Q-factor produces a narrower bandwidth and a sharper frequency response peak near the center frequency, which contributes to a higher device sensitivity. For a

SAW device, once the f_0 is fixed, both the Q-factor and bandwidth are dependent on the numbers of finger pairs N_p of the input IDT. The approximate relation between them is developed by (Bell & Li, 1976):

$$\Delta f = \frac{2f_0}{N_p} \tag{2.14}$$

In other words, the Q-factor is in inverse proportion to the Δf, whereas the direct ratio to the N_p. However, it is impractical to just keep increasing the numbers of finger pair without limit since a large N_p can lead to a high device resistance and excessive insertion loss.

Knowing that the parameters mentioned above reveal the device performance in different aspects, the designing process should consider all the factors that may contribute to the overall device performance, and some compromises are hence required. Also, an optimization process can be done by altering the originally designed constants of the device dimensions and material such as the acoustic aperture, finger thickness, delay line distance, and the material selections for both IDT and substrate, which are directly or indirectly related to the performance parameters. A theoretical modeling approach accompanied by the numerical tool is implemented in the following chapters to evaluate the performance of the designed SAW sensor and provide possible optimization.

2.6. Summary

The chapter first brings out the basic knowledge of piezoelectricity, including its mechanism, constitutive equations, material types, processing approach, and effect on the corresponding Rayleigh wave. A two-port SAW-DL sensor as the thesis's main object is then emphatically introduced with its working principles and configurations. The sensor

design is involved with the factors from both IDT and piezoelectric substrate. Several parameters that are related to the sensor's dimensions, material properties, and performance are presented and discussed for the possible ideas of better design and optimization.

3. Theoretical Modeling of SAW Sensor

To design high-performance SAW devices, precise and efficient modeling tools are required. Several methods have been proposed for modeling such as the impulse response model, equivalent circuit model, and coupling of modes (COM) model, in which the COM model is widely accepted for modeling the SAW device due to its excellent advantages.

In this chapter, the modeling processes of the SAW device are performed basing on the COM model and using the MATLAB algorithm to obtain its frequency response. The MATLAB models the SAW device by cascading the transmission matrices of its different components which can be an IDT, delay line, or reflector. The COM model is used to derive the expression of each transmission matrix.

3.1. Principle of COM Model

The coupling of modes (COM) model shows the extraordinary capability of analyzing the microwave and optical structures with distributed reflections. It is initially developed to settle the difficulty that the existing models are not applied to a specific type of SAW devices such as single-phase unidirectional transducer (SPUDT). In 1989, a novel general COM analysis of SAW transducers and gratings is raised by (Wright, 1989). Despite that many further modified works of the COM model for SAW devices are done, the basic COM differential equations we use today, which are a set of first-order wave equations, are still following the similar principle of Wright's work.

In this section, an overall process of COM analysis is presented. A detailed derivation of the general COM differential equations for a SAW reflector is first developed. With applied voltage and current onto the gratings, a SAW IDT model is performed by adding

another COM differential equation and coupling the electrical port with acoustic ports. Exact solutions for the different components of a SAW device can be obtained by using numerical methods to solve the COM equations. In order to get the response of the entire device, a cascading approach using MATLAB is performed in the next section.

3.1.1. COM First Order Differential Wave Equations

The COM model is a one-dimension analysis that models the propagating waves as scaler waves (Abbott, 1991). A SAW reflector is a set of periodic reflective and conductive strips laying on the piezoelectric substrates, which have two acoustic ports. Figure 3.1 shows a schematic of two acoustic waves, $r(x,t)$ and $s(x,t)$, propagating in the forward and backward modes.

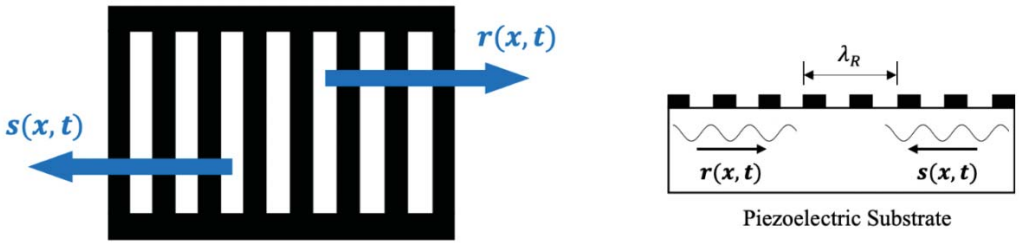

Figure 3.1 The top and side views of the SAWs propagating through the reflector gratings.

These two waves are initially uncoupled and unperturbed before the presence of the gratings, whose wave equations in the time domain are described as follows:

$$\frac{dr(x,t)}{dx} = -\frac{1}{v_R(x,\omega)}\frac{dr(x,t)}{dt} \tag{3.1}$$

$$\frac{ds(x,t)}{dx} = +\frac{1}{v_R(x,\omega)}\frac{ds(x,t)}{dt} \tag{3.2}$$

where $v_R(x,\omega)$ denotes the spatially and frequency-dependent velocity of the Rayleigh wave. Because the wave propagating through the reflector gratings is frequency-dependent, the first-order wave equations in the frequency domain are derived using the Fourier transform as:

$$\frac{dR(x,\omega)}{dx} = -jk_R(x,\omega)R(x,\omega) \tag{3.3}$$

$$\frac{dS(x,\omega)}{dx} = +jk_R(x,\omega)\,S(x,\omega) \tag{3.4}$$

where the Rayleigh wavenumber is given by:

$$k_R(x,\omega) = \frac{2\pi}{\lambda_R} = \frac{\omega}{v_R(x,\omega)} \tag{3.5}$$

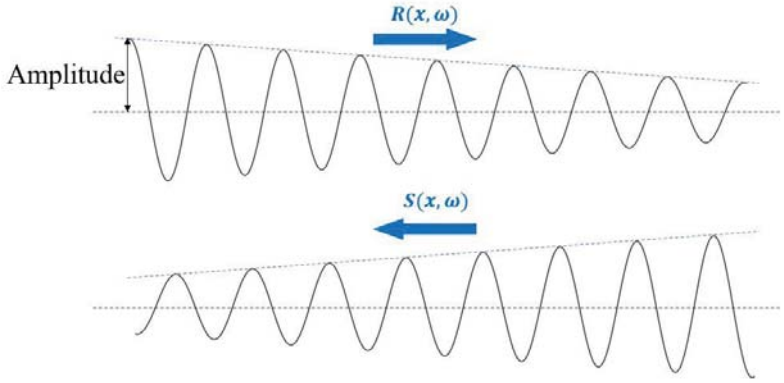

Figure 3.2 Wave attenuation along the propagating directions.

3.1.2. Characteristics of Perturbation and Coupling

As the presence of the gratings, several perturbing and coupling effects (e.g., SAW attenuation, acoustic reflection, and SAW velocity variation) are taken into consideration and added to the initial wave equations, respectively.

The propagation loss occurs in the lossy structures, which can be presented by an amplitude attenuation of the forward and backward propagating waves, as shown in Figure 3.2.

A spatially and frequency-dependent attenuation parameter $\alpha(x,\omega)$ is added to the wave equations, which is given by Equation 3.6-3.7. The sign convention for the attenuation parameter is consistent with the slopes of the decaying waves in Figure 3.2.

$$\frac{dR(x,\omega)}{dx} = -jk_R(x,\omega)R(x,\omega) - \alpha(x,\omega)R(x,\omega) \tag{3.6}$$

$$\frac{dS(x,\omega)}{dx} = +jk_R(x,\omega)S(x,\omega) + \alpha(x,\omega)S(x,\omega) \tag{3.7}$$

The acoustic reflection happens due to the presence of metal strips. Once encountering the strips, both of the forward and backward waves collect the partially reflected waves from the opposite directions, thus forming a coupling between two waves. To model the effect of acoustic reflection and insert it into the wave equations, a numerical analysis based on the periodic impedance variation (discontinuity) is developed by (Abbott, 1991). As a result, a reflection parameter $\gamma(x,\omega)$ (varies in different directions) is defined and its expression is derived in terms of the spatially and frequency-dependent impedance of the overall SAW structure.

The variation of the wave velocity is on account of the mass loading and electrical shorting of the metal strips, which alter the natural frequency of the Rayleigh wave on the piezoelectric substrate. An average velocity $v_R'(x,\omega)$ that includes the effects of the mass loading $\Delta v_m(x,\omega)$ and electrical shorting $\Delta v_e(x,\omega)$ is defined, and the corresponding average wave number $k_R'(x,\omega)$ is updated in the new wave equations. Besides, there's no

need to concern the difference between the phase and group velocity since the surface acoustic wave is non-dispersive.

A couple of modified wave equations become:

$$\frac{dR(x,\omega)}{dx} = -j[k'_R(x,\omega) - j\alpha(x,\omega)]R(x,\omega) + \gamma_R(x,\omega)S(x,\omega) \tag{3.8}$$

$$\frac{dS(x,\omega)}{dx} = +j[k'_R(x,\omega) - j\alpha(x,\omega)]S(x,\omega) - \gamma_S(x,\omega)R(x,\omega) \tag{3.9}$$

where $k'_R(x,\omega)$ is given as:

$$k'_R(x,\omega) = \frac{\omega}{v'_R(x,\omega)} = \frac{\omega}{v_R(x,\omega) + \Delta v_m(x,\omega) + \Delta v_e(x,\omega)} \tag{3.10}$$

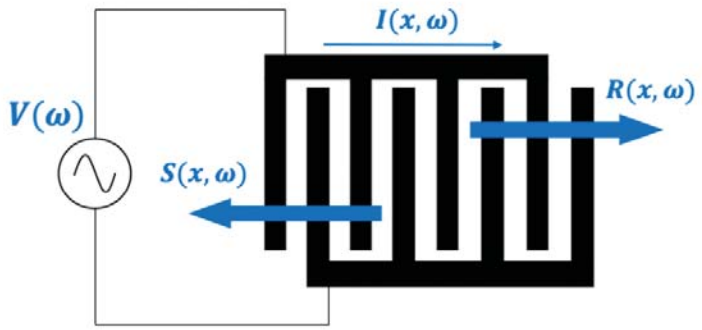

Figure 3.3 Schematic of a single-finger IDT model with three ports.

3.1.3. COM Equations for a SAW IDT

Unlike the reflector model, the SAW IDT is applied by an alternating voltage and current as shown in Figure 3.3, which causes a third COM differential equation describing the additional electrical port and as a transduction parameter $\xi(x,\omega)$ coupling

the electrical and acoustic ports. Beyond that, two more perturbing effects are introduced for the IDT model which are finger resistance and capacitance.

A set of concise expressions of the COM differential equations for a 3-port SAW IDT are established as:

$$\frac{dR(x,\omega)}{dx} = -j\delta(x,\omega)R(x,\omega) + \gamma_R(x,\omega)S(x,\omega) + j\xi_R(x,\omega)V(\omega) \tag{3.11}$$

$$\frac{dS(x,\omega)}{dx} = +j\delta(x,\omega)S(x,\omega) - \gamma_S(x,\omega)R(x,\omega) - j\xi_S(x,\omega)V(\omega) \tag{3.12}$$

$$\frac{dI(x,\omega)}{dx} = 2j\xi_S R(x,\omega) + 2j\xi_R S(x,\omega) - j\omega\psi(x,\omega)V(\omega) \tag{3.13}$$

where $\delta(x,\omega) = k_R'(x,\omega) - j\alpha(x,\omega)$ is the detuning parameter, and $\psi(x,\omega)$ is dependent on the electrode resistance and capacitance, and the dimensional parameters of the IDT. More detailed expressions for each parameter are derived explicitly in (Abbott, 1991) and then used to solve the numerical solutions for the SAW devices.

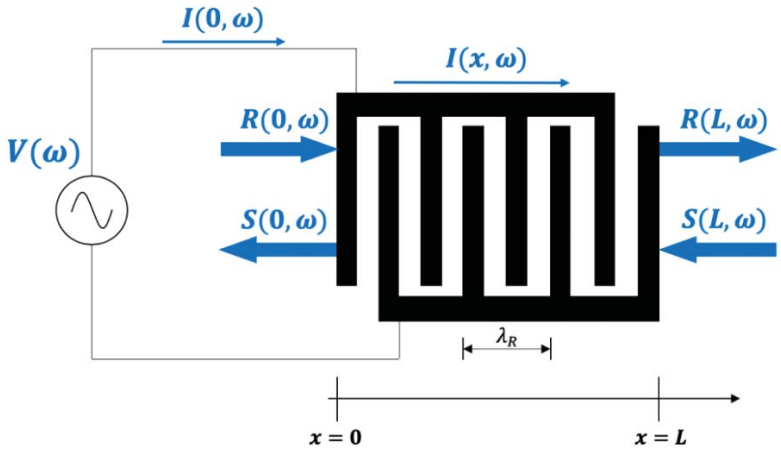

Figure 3.4 Boundary conditions of a uniform SAW IDT.

3.1.4. P-Matrix Representation of a Uniform SAW Component

A derivation of the solutions for a uniform SAW device is presented here since the IDT used in this thesis is uniformly designed. Further solutions for a general device can be done by cascading the solutions of each uniform component in the matrix form.

As shown in Figure 3.4, boundary conditions (BCs) are applied onto the SAW IDT compared with Figure 3.3. $R(0,\omega)$ and $S(L,\omega)$ represent the two incident waves before encountering the perturbations, and $R(L,\omega)$ and $S(0,\omega)$ are the leaving waves. By applying the alternating voltage $V(\omega)$ as the input, a terminal current $I(0,\omega)$ is propagating through the bus bars and fingers as spatially dependent current $I(x,\omega)$. Because the IDT is assumed to be uniform, all the COM parameters (i.e., k_R, α, γ, and ξ) become only frequency-dependent, whereas spatially independent.

The BCs come to:

$$R(0,\omega) = R_{in} \tag{3.14}$$

$$S(L,\omega) = S_{in} \tag{3.15}$$

$$V(\omega) = V_0 \tag{3.16}$$

where R_{in} and S_{in} stand for the amplitude of incident counter-propagating waves, and V_0 is the applied voltage. These three values are set as constants in the expressions of the general solutions, and the pair of bus bars are assumed to be lossless. The exact solutions of $R(x,\omega)$, $S(x,\omega)$ and $I(x,\omega)$ are developed in previous works (Abbott, 1991; Chen & Haus, 1985; Wright, 1989). Due to the huge numerical procedure, the full expression for each port is not presented here. Only the results of leaving waves, $R(L,\omega) = R_{out}$,

$S(0,\omega) = S_{out}$ and the terminal current, $I(0,\omega) = I_0$, are taken into account, as they are the essential characteristics of a uniform IDT.

A P-matrix notation is introduced in (Tobolka, 1979) that relates both the incident and leaving waves, and acoustic ports and electrical port. The P-matrix representation is shown as:

$$\begin{bmatrix} S_{out} \\ R_{out} \\ I_0 \end{bmatrix} = \begin{bmatrix} P_{11} & P_{12} & P_{13} \\ P_{21} & P_{22} & P_{23} \\ P_{31} & P_{32} & P_{33} \end{bmatrix} \begin{bmatrix} R_{in} \\ S_{in} \\ V_0 \end{bmatrix} \tag{3.17}$$

where P_{11}, P_{22}, and the P_{12}, P_{22} are the acoustical scattering parameters representing the reflection and transfer, respectively. This $2x2$ scattering matrix can be defined as the description of the wave interaction of an electrically short structure ($V_0 = 0$) such as a reflector. P_{33} is the admittance parameter coupling the current and applied voltage when there are no acoustic inputs ($R_{in} = S_{in} = 0$). P_{13} and P_{23} are acoustic-electrical parameters. The expressions of the P-matrix elements are derived in (Abbott, 1991) based on the solutions of the COM model. Besides, they also follow the reciprocity relations as:

$$P_{12} = P_{21}, P_{31} = -2P_{13}, P_{32} = -2P_{23} \tag{3.18}$$

3.2. MATLAB Analysis Based on COM Model

As the exact solutions for a uniform SAW IDT are discussed above, the main idea to simulate the response of an overall non-uniform SAW device comes to cascading the discrete uniform components.

3.2.1. Transmission Matrix Representation

Although the P-matrix is available for cascading (Abbott, 1991), it is not convenient enough for cascading different element types (e.g., reflector, IDT, and delay line). To make the simulation compute fast and fulfill the capability of parametric optimization, a modified transmission matrix representation based on the conventional P-matrix is developed in (Morgan, 1996; Ro et al., 2004):

$$\begin{bmatrix} S_{n-1} \\ R_{n-1} \\ I \end{bmatrix} = \begin{bmatrix} t_{11} & t_{12} & t_{13} \\ t_{21} & t_{22} & t_{23} \\ t_{31} & t_{32} & t_{33} \end{bmatrix} \begin{bmatrix} R_n \\ S_n \\ V \end{bmatrix} \tag{3.19}$$

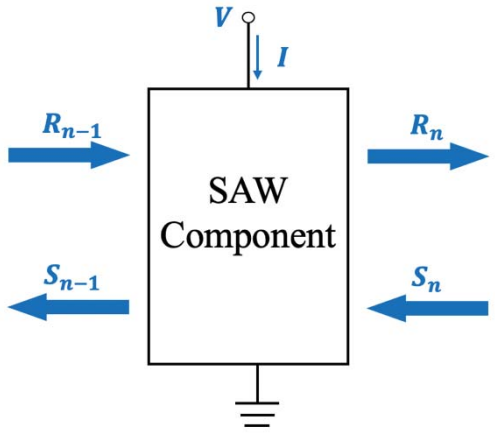

Figure 3.5 A three-port transmission line with two acoustic fields and one electrical field.

The transmission matrix relates the acoustic fields to the left and right sides and deals with the electrical field within the object of study, as shown in Figure 3.5. A significant advantage of this approach is that it can model not only a SAW component but also a single element such as an electrode or free spacing. The elements of the transmission matrix obey the relations with P-matrix as:

$$t_{11} = P_{21} - \frac{P_{22}P_{11}}{P_{12}}, t_{12} = \frac{P_{22}}{P_{12}}, t_{13} = P_{23} - \frac{P_{22}P_{13}}{P_{12}}$$
$$t_{21} = -\frac{P_{11}}{P_{12}}, t_{22} = \frac{1}{P_{12}}, t_{23} = P_{23} - \frac{P_{13}}{P_{12}} \quad (3.20)$$
$$t_{31} = P_{31} - \frac{P_{32}P_{11}}{P_{12}}, t_{32} = \frac{P_{32}}{P_{12}}, t_{33} = P_{33} - \frac{P_{32}P_{13}}{P_{12}}$$

3.2.2. Building Blocks and Cascading Procedures

A set of building blocks for a general 2-port SAW device is introduced in Figure 3.6 to explain the flow path and algorithm of the simulation. The matrices $[G]$, $[T]$ and $[D]$ represent the transmission matrices of the reflective gratings, IDTs, and delay lines, respectively. In this section, a SAW system consisting of two IDTs and a delay line between them is discussed. A set of solutions for this system are derived in the following.

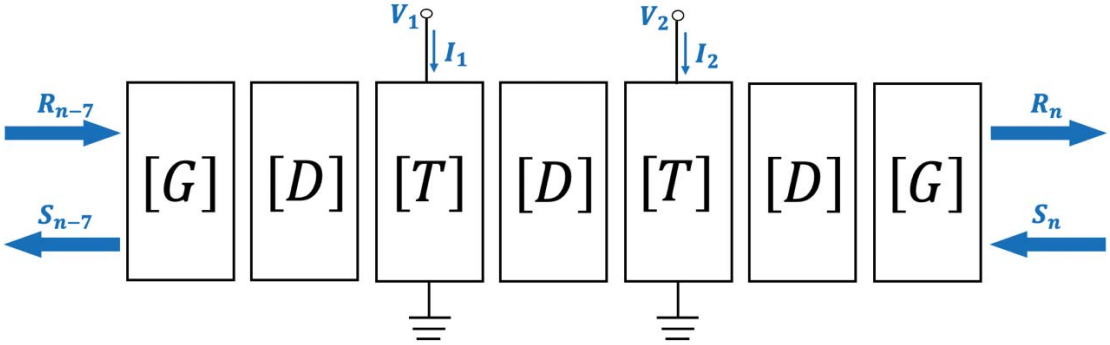

Figure 3.6 Building blocks of a SAW transmission system.

The delay line is assumed to be a 2-port component, and no perturbation is applied. The solution for the delay line matrix is given as:

$$[D] = \begin{bmatrix} e^{jkd} & 0 \\ 0 & e^{-jkd} \end{bmatrix} \quad (3.21)$$

where k denotes the wavenumber and d is the length of the delay line.

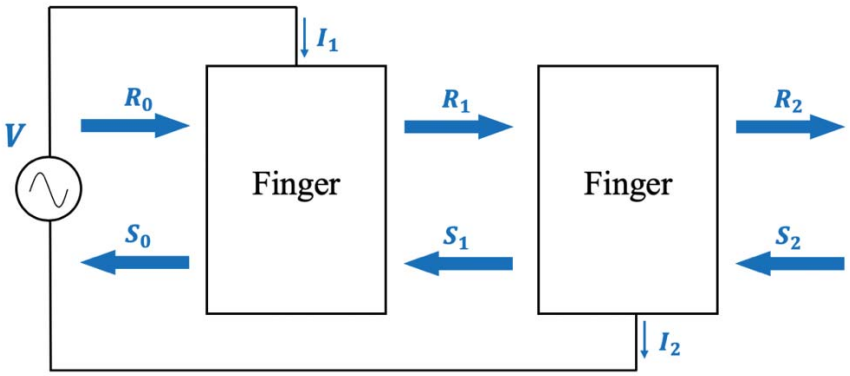

Figure 3.7 Building blocks of a finger pair cascaded.

The idea to obtain the transmission matrix for an IDT is to split the IDT into several periodic units, cascade them, and conclude the general law for each element of the overall transmission matrix. The building blocks of a finger pair are shown in Figure 3.7, whose individual transmission matrix equations are presented in Equation 3.22 and 3.23. The purpose of analyzing the transmission properties of a finger pair is to develop a MATLAB algorithm for simulating the IDT structure.

$$\begin{bmatrix} S_0 \\ R_0 \\ I_1 \end{bmatrix} = \begin{bmatrix} t_{11} & t_{12} & t_{13} \\ t_{21} & t_{22} & t_{23} \\ t_{31} & t_{32} & t_{33} \end{bmatrix} \begin{bmatrix} R_1 \\ S_1 \\ V \end{bmatrix} \tag{3.22}$$

$$\begin{bmatrix} S_1 \\ R_1 \\ I_2 \end{bmatrix} = \begin{bmatrix} t_{11} & t_{12} & t_{13} \\ t_{21} & t_{22} & t_{23} \\ t_{31} & t_{32} & t_{33} \end{bmatrix} \begin{bmatrix} R_2 \\ S_2 \\ V \end{bmatrix} \tag{3.23}$$

These 3-port matrices can be split into a 2-port and 1-port representations:

$$\begin{bmatrix} R_0 \\ S_0 \end{bmatrix} = \begin{bmatrix} t_{11} & t_{12} \\ t_{21} & t_{22} \end{bmatrix}_1 \begin{bmatrix} R_1 \\ S_1 \end{bmatrix} + \begin{bmatrix} t_{13} \\ t_{23} \end{bmatrix}_1 V \tag{3.24}$$

$$I_1 = [t_{31} \quad t_{32}]_1 \begin{bmatrix} R_1 \\ S_1 \end{bmatrix} + (t_{33})_1 V \tag{3.25}$$

$$\begin{bmatrix} R_1 \\ S_1 \end{bmatrix} = \begin{bmatrix} t_{11} & t_{12} \\ t_{21} & t_{22} \end{bmatrix}_2 \begin{bmatrix} R_2 \\ S_2 \end{bmatrix} + \begin{bmatrix} t_{13} \\ t_{23} \end{bmatrix}_2 V \tag{3.26}$$

$$I_2 = [t_{31} \quad t_{32}]_2 \begin{bmatrix} R_2 \\ S_2 \end{bmatrix} + (t_{33})_2 V \tag{3.27}$$

By cascading the two fingers, the transmission matrices for a finger pair become:

$$\begin{bmatrix} R_0 \\ S_0 \end{bmatrix} = \begin{bmatrix} t_{11} & t_{12} \\ t_{21} & t_{22} \end{bmatrix}_1 \begin{bmatrix} t_{11} & t_{12} \\ t_{21} & t_{22} \end{bmatrix}_2 \begin{bmatrix} R_2 \\ S_2 \end{bmatrix} + \left(\begin{bmatrix} t_{11} & t_{12} \\ t_{21} & t_{22} \end{bmatrix}_1 \begin{bmatrix} t_{13} \\ t_{23} \end{bmatrix}_1 + \begin{bmatrix} t_{13} \\ t_{23} \end{bmatrix}_1 \right) V \tag{3.28}$$

$$\begin{aligned} I = I_1 + I_2 = [t_{31} \quad t_{32}]_1 \left(\begin{bmatrix} t_{11} & t_{12} \\ t_{21} & t_{22} \end{bmatrix}_2 \begin{bmatrix} R_2 \\ S_2 \end{bmatrix} + \begin{bmatrix} t_{13} \\ t_{23} \end{bmatrix}_2 V \right) \\ + [t_{31} \quad t_{32}]_2 \begin{bmatrix} R_2 \\ S_2 \end{bmatrix} + (t_{33})_1 V + (t_{33})_2 V \end{aligned} \tag{3.29}$$

In order to express the overall transmission matrix for a finger pair and further to be the whole IDT, a new representation is introduced:

$$[T]_{3\times3} = \begin{bmatrix} Q_{2\times2} & B_{2\times1} \\ C_{1\times2} & A_{1\times1} \end{bmatrix} \tag{3.30}$$

Comparing the expressions between Equation 3.28 and 3.24, and Equation 3.29 and 3.25, the cascading forms for the new transmission matrix representation are:

$$[Q]_{fp} = \begin{bmatrix} t_{11} & t_{12} \\ t_{21} & t_{22} \end{bmatrix}_{fp} = \begin{bmatrix} t_{11} & t_{12} \\ t_{21} & t_{22} \end{bmatrix}_1 \begin{bmatrix} t_{11} & t_{12} \\ t_{21} & t_{22} \end{bmatrix}_2 \tag{3.31}$$

$$[C]_{fp} = [t_{31} \quad t_{32}]_{fp} = [t_{31} \quad t_{32}]_1 \begin{bmatrix} t_{11} & t_{12} \\ t_{21} & t_{22} \end{bmatrix}_2 + [t_{31} \quad t_{32}]_2 \tag{3.32}$$

$$[B]_{fp} = \begin{bmatrix} t_{13} \\ t_{23} \end{bmatrix}_{fp} = \begin{bmatrix} t_{11} & t_{12} \\ t_{21} & t_{22} \end{bmatrix}_1 \begin{bmatrix} t_{13} \\ t_{23} \end{bmatrix}_2 + \begin{bmatrix} t_{13} \\ t_{23} \end{bmatrix}_1 \tag{3.33}$$

$$A_{fp} = (t_{33})_{fp} = [t_{31} \quad t_{32}]_1 \begin{bmatrix} t_{13} \\ t_{23} \end{bmatrix}_2 + (t_{33})_1 + (t_{33})_2 \tag{3.34}$$

Then, the final transmission matrix for an nth-finger-pair IDT can be concluded as:

$$[T]_N = \begin{bmatrix} Q_N & B_N \\ C_N & A_N \end{bmatrix} \tag{3.35}$$

where

$$[Q]_N = \left([Q]_{fp}\right)^N \tag{3.36}$$

$$[C]_N = \sum_{i=0}^{N-1} [Q]_{fp}^i \, [C]_{fp} \tag{3.37}$$

$$[B]_N = \sum_{i=0}^{N-1} [Q]_{fp}^i \, [B]_{fp} \tag{3.38}$$

$$A_N = \sum_{i=1}^{N} (N-i)[C]_{fp}[Q]_{fp}^{i-1} \, [B]_{fp} \tag{3.39}$$

Obtaining the matrix expressions of both delay line and IDT, an integrated transmission matrix for a 3-component SAW device, as shown in figure 3.8, is developed in (Krishnamurthy, 2007). The relations between the left and right sides of the device for both acoustic and electrical ports are written as:

$$\begin{bmatrix} R_0 \\ S_0 \end{bmatrix} = [Q]_{in}[D][Q]_{out} \begin{bmatrix} R_3 \\ S_3 \end{bmatrix} + [B]_{in}V_{in} + [Q]_{in}[D][B]_{out}V_{out} \tag{3.40}$$

$$I_{in} = [C]_{in}[D][Q]_{out}\begin{bmatrix} R_3 \\ S_3 \end{bmatrix} + [C]_{in}[D][B]_{out}V_{out} + A_{in}V_{in} \tag{3.41}$$

$$I_{out} = [C]_{out}\begin{bmatrix} R_3 \\ S_3 \end{bmatrix} + A_{out}V_{out} \tag{3.42}$$

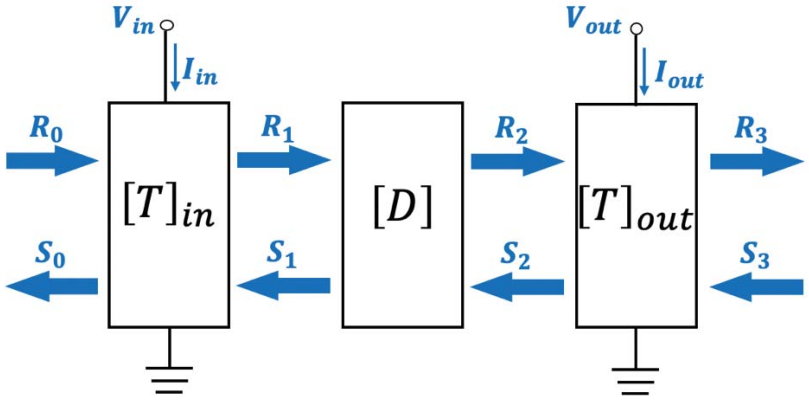

Figure 3.8 The transmission line of a three-component SAW device.

As the final goal of the MATLAB analysis is to plot the specific scattering parameter (S-parameter) for the overall device, an admittance (Y-parameter) matrix representation is first brought here:

$$\begin{bmatrix} I_{in} \\ I_{out} \end{bmatrix} = \begin{bmatrix} Y_{11} & Y_{12} \\ Y_{21} & Y_{22} \end{bmatrix}\begin{bmatrix} V_{in} \\ V_{out} \end{bmatrix} \tag{3.43}$$

Each individual element of the admittance matrix can be derived by combining Equation 3.40-3.43. The results are shown as:

$$Y_{11} = -\frac{(T_{31})_{in}e^{jkd}(T_{11})_{out} + (T_{32})_{in}e^{-jkd}(T_{21})_{out}}{(T_{12})_{in}e^{jkd}(T_{11})_{out} + (T_{12})_{in}e^{-jkd}(T_{21})_{out}}(T_{13})_{in} + (T_{33})_{in} \tag{3.44}$$

$$Y_{21} = -\frac{(T_{13})_{out}(T_{13})_{in}}{(T_{12})_{in}e^{jkd}(T_{11})_{out} + (T_{12})_{in}e^{-jkd}(T_{21})_{out}} \tag{3.45}$$

$$
\begin{aligned}
Y_{12} = -\big[&(T_{31})_{in}e^{jkd}(T_{11})_{out} \\
&+ (T_{32})_{in}e^{-jkd}(T_{21})_{out}\big]\big[(T_{11})_{in}e^{jkd}(T_{13})_{out} \\
&+ (T_{12})_{in}e^{-jkd}(T_{23})_{out}\big]\big[(T_{12})_{in}e^{jkd}(T_{11})_{out} \\
&+ (T_{12})_{in}e^{-jkd}(T_{21})_{out}\big]^{-1} + (T_{31})_{in}e^{jkd}(T_{13})_{out} \\
&+ (T_{32})_{in}e^{-jkd}(T_{23})_{out}
\end{aligned}
\tag{3.46}
$$

$$
Y_{22} = -\frac{(T_{13})_{out}\big[(T_{11})_{in}e^{jkd}(T_{13})_{out} + (T_{12})_{in}e^{-jkd}(T_{23})_{out}\big]}{(T_{12})_{in}e^{jkd}(T_{11})_{out} + (T_{12})_{in}e^{-jkd}(T_{21})_{out}} + (T_{33})_{out} \tag{3.47}
$$

The final step is to convert the Y-parameters to the S-parameters. Only the S_{11} and S_{21} are discussed here due to their essential roles in presenting the frequency responses, whose expression comes to:

$$
S_{11} = \frac{(1 - Z_1^* Y_{11})(1 + Z_2 Y_{22}) - Y_{21} Y_{12} Z_2 Z_2^*}{(1 + Z_1 Y_{11})(1 + Z_2 Y_{22}) - Z_1 Y_{12} Z_2 Y_{21}} \tag{3.48}
$$

$$
S_{21} = \frac{-2\sqrt{R_1 R_2} Y_{21}}{(1 + Z_1 Y_{11})(1 + Z_2 Y_{22}) - Z_1 Y_{12} Z_2 Y_{21}} \tag{3.49}
$$

where $Z_1$and Z_2 stand for the complex characteristic impedance of both ports as shown in Figure 3.9, and R_1 and R_2 are the real parts of the impedance, respectively.

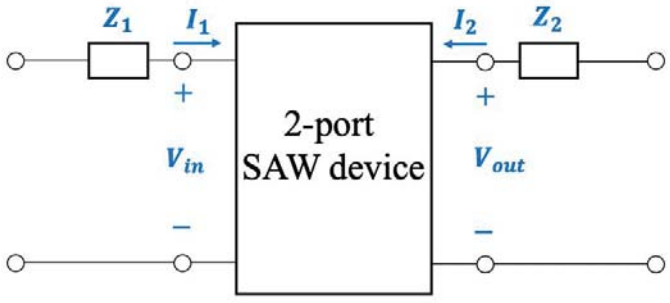

Figure 3.9 A two-port SAW device with two characteristic impedance.

The entire contents of the MATLAB algorithm are listed in Appendix-A. All the input constants in the algorithm, which are related to the device dimensions, wave properties, and material properties, are given in the following chapter. The theoretical modeling result is compared with the numerical analysis to validate the reliability of both approaches.

3.3. Summary

In summary, this theoretical modeling method that combines both COM theory and transmission matrix approach has quite a few outstanding advantages: 1) it is efficient and flexible for modeling various types of SAW devices and the assembly of non-uniform transducers; 2) it considers a wide range of perturbation effects that makes the solution more accurate and trustier; 3) it enables extremely little computational time which is to the benefit of fast optimization. However, because the COM model analyzes the waves with the wavelength equal to the IDT period, the COM solutions are only accurate within a certain bandwidth near its center (fundamental) frequency.

4. Numerical Analysis of SAW Sensor

The theoretical modeling usually has some limitations compared to the numerical analysis. The numerical analysis solves the device directly from the complexities of material constants, the device dimensions, and the boundary conditions as well as the applied external loads, which the theoretical modeling may not be able to cover. Thus, numerical analysis is potentially closer to real-life applications than theoretical modeling.

In this chapter, an integrated SAW sensor geometry is built and numerically analyzed in COMSOL Multiphysics software. By applying proper boundary conditions and input electrical signals, the sensor responses in both time and frequency domains are obtained and presented with conclusions. A comparison with theoretical modeling is also exhibited to verify the results. At the end of this chapter, the performances between two different types of piezoelectric materials as the substrate are discussed.

4.1. Introduction of COMSOL Multiphysics

COMSOL Multiphysics provides a dominant simulation environment for the models interacted with multiple physical types, as well as a concise graphical user interface. It works by following the rules of the partial differential equations (PDEs), which are the basic principles of the scientific phenomena and couplings of multiple physics.

This study adopts COMSOL due to its decent and dedicated piezoelectricity interface (Multiphysics, 2008), making it a better choice for simulating the SAW-based devices. The piezoelectricity interface couples the two physics of solid mechanics and electrostatics following the principle of piezoelectric constitution equations for both direct and converse effects. For this application area, certain add-on modules are required. The MEMS (microelectromechanical system) module is standing out here for

the simulation of a piezoelectric device. It has numerous features, e.g., piezoelectricity, electrostatics, and thermal interfaces, which cover a wide range of tools to achieve simulating the microsystems. Besides, it is able to evaluate multiple useful solutions for SAW device responses, such as lumped parameters (S-parameters, Z-parameters, Y-parameters) and circuit parameters.

For analyzing a piezoelectric structure in COMSOL, the material properties conventions need to be clear. The COMSOL requires three particular properties for a piezoelectric material: the stiffness (or compliance) matrix, piezoelectric coupling matrix, and permittivity (dielectric) matrix. They are defined in a coordinate system that consists of three axes in the notation of 1, 2, and 3. The poling direction is the key to the piezoelectric performance. In COMSOL, the poling direction is defaulted along the 3rd axis (Z-axis for the global coordinate system). If a piezoelectric material has irregular poling direction, the COMSOL provides a rotated coordinate system based on the Euler angles' rule to modify the model along with any material orientation.

4.2. Modeling of SAW Sensor in COMSOL

A two-port SAW-DL sensor geometry is built in the COMSOL, as shown in Figure 4.1. The length and width of the substrate are along the x and y-axes, respectively, and the thickness is towards the z-axis, which meets the exact poling direction for the chosen piezoelectric substrate. A couple of single-finger IDTs with the period p=300 μm and the metallized ratio η=0.5 are designed to meet the operating frequency near 2.5 MHz. The substrate is set to have 500 μm height in order to perform the surface wave flawlessly, and it is also thin enough to cut down the computational time.

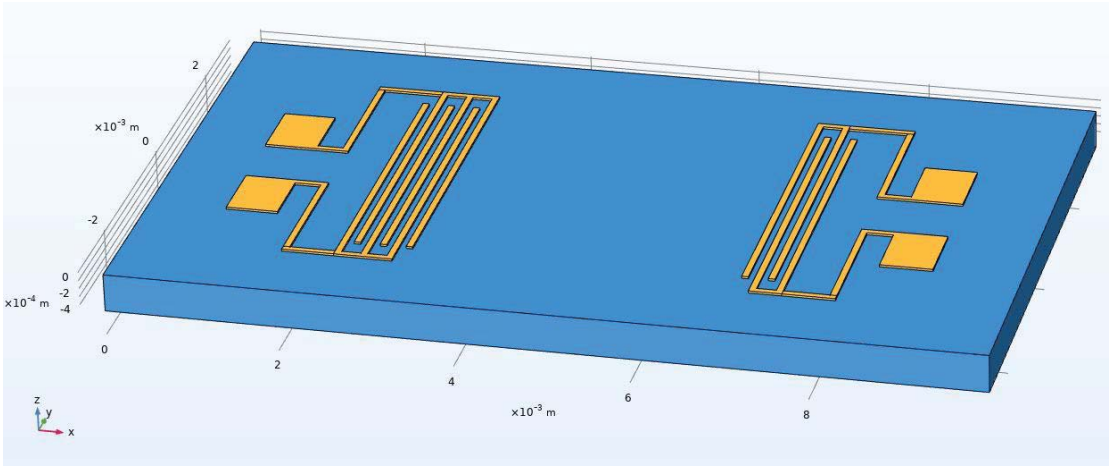

Figure 4.1 A COMSOL SAW-DL sensor geometry with a poling direction along the z-axis.

Table 4.1

Dimensional parameters of the designed SAW sensor.

Dimension	**Value**
Finger width (free space width) [μm]	75 (75)
Wavelength [μm]	300
Substrate height [μm]	500
Delay line distance [mm]	4.5
No. input (output) finger pair	3 (2)
Acoustic aperture [mm]	3.5
Finger thickness [μm]	25

The delay line distance refers to the IDTs' center-to-center space which is chosen to be 4.5 *mm* to acquire a sufficient delay in time-domain analysis; meanwhile, to be short enough to reduce the unnecessary signal decay. The finger thickness is firstly set as 25 μm to keep the balance between large resistance and mass loading. To begin with, the numbers of input and output finger pairs are originally maintained to be 3 and 2,

respectively. The acoustic aperture is initially kept as 3.5 *mm*, which can be altered during the optimization process and the No. finger pair and finger thickness. A list of the overall sensor dimensions is shown in Table 4.1.

Table 4.2

Material properties of the PVDF-based SAW sensor (Comsol, 2007).

Material	**Description [unit]**	**Value**
Structural steel (IDT material)	Density ρ [kg/m^3]	7,850
	Young's modulus E [GPa]	200
	Poisson's ratio υ	0.3
Polyvinylidene fluoride (PVDF)	Density ρ [kg/m^3]	1,780
	Young's modulus E [GPa]	3
	Poisson's ratio υ	0.24
	Elastic compliance matrix s^E [$10^{-10}\cdot Pa^{-1}$]	$\begin{bmatrix} 3.781 & -1.482 & -1.724 & 0 & 0 & 0 \\ -1.482 & 3.781 & -1.724 & 0 & 0 & 0 \\ -1.724 & -1.724 & 10.92 & 0 & 0 & 0 \\ 0 & 0 & 0 & 14.28 & 0 & 0 \\ 0 & 0 & 0 & 0 & 11.1 & 0 \\ 0 & 0 & 0 & 0 & 0 & 11.1 \end{bmatrix}$
	Piezoelectric-strain matrix d [$10^{-12}\cdot C/N$]	$\begin{bmatrix} 0 & 0 & 0 & 0 & 0 & 0 \\ 0 & 0 & 0 & 0 & 0 & 0 \\ 13.58 & 1.476 & -33.8 & 0 & 0 & 0 \end{bmatrix}$
	Permittivity matrix ε_r^S	$\begin{bmatrix} 7.4 & 0 & 0 \\ 0 & 9.3 & 0 \\ 0 & 0 & 7.74 \end{bmatrix}$
	Curie temperature T_c [$°C$]	195
	Electromechanical coupling factor k^2	0.14

As one of the most popular piezoelectric polymers, Polyvinylidene Fluoride (PVDF) has recently gained significant interest in the material selection for piezoelectric sensors

due to its excellent flexibility and reproductivity, as well as the high sensitivity to physical changes. PVDF is initially chosen as the substrate material, and its critical properties for simulating the piezoelectric model are listed in Table 4.2.

COMSOL solves the full solid mechanics model based on those critical material properties. All the wave modes, such as P-wave, S-wave, and Rayleigh wave, are simulated simultaneously, and the different wave velocities are calculated automatically by the in-build numerical algorithm. When running a transient analysis in the time domain using a short pulse excitation, different wave modes may be separated after traveling some distance because of their velocity differences.

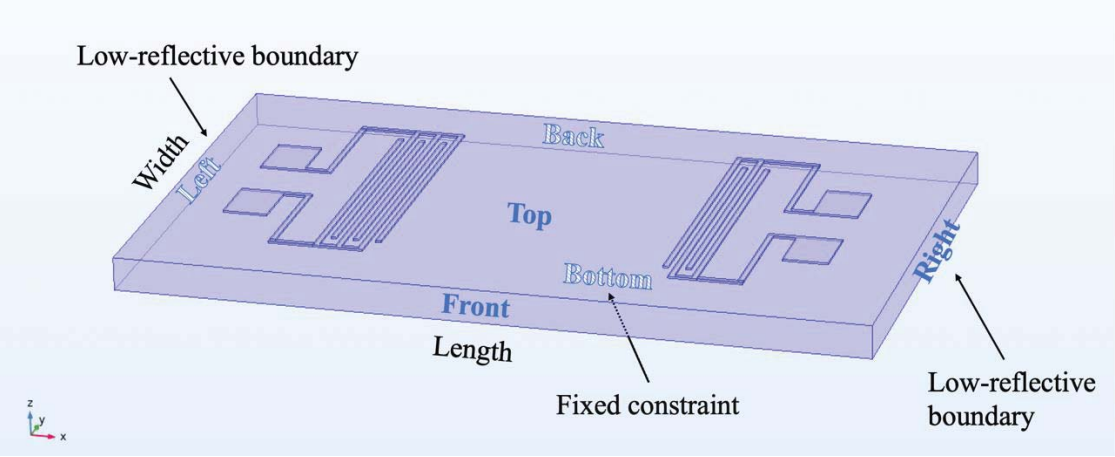

Figure 4.2 Boundary conditions of the SAW sensor model in a transparent view.

The boundary conditions (BCs) are essential to the numerical solutions. The length and width of the substrate are reduced to 10 and 6 *mm*, respectively, for cutting down the computational time. A “low-reflective boundary condition” feature is assigned to the left and right boundaries to simulate the effects of a couple of absorbers or grating reflectors, which are usually placed near the two edges of the top substrate to eliminate the reflecting interference. The bottom surface of the substrate is fixed to simulate the

bonding with the host structure. The front and back boundaries, as well as the top surface, are free for constraint.

Two components (IDT and substrate) of the SAW sensor are meshed using the tetrahedral element with the size of $\lambda/8$ and $\lambda/3$, respectively, and 574429 domain elements, 60018 boundary elements, and 5340 edge elements are obtained for the whole model.

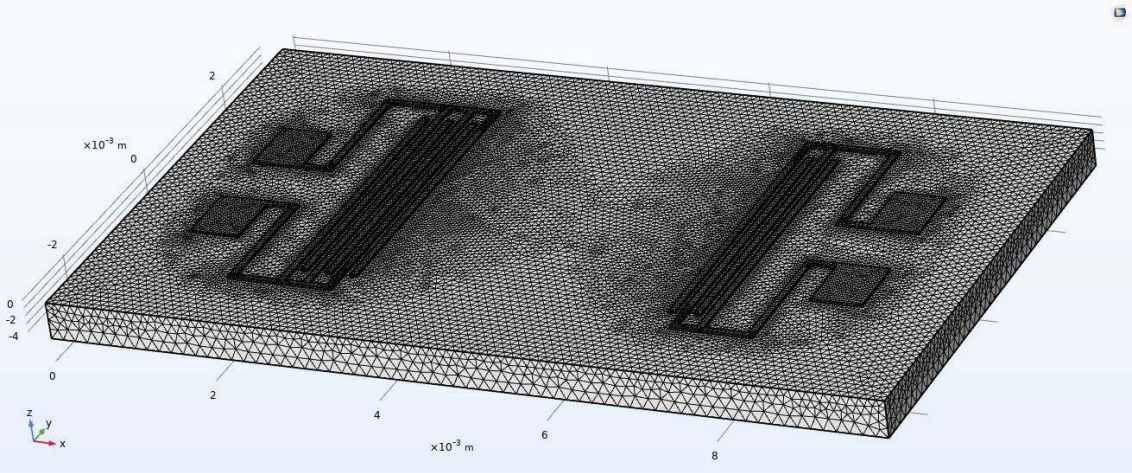

Figure 4.3 Meshed condition of the SAW sensor model.

4.3. Time Domain Analysis

In this section, a transient analysis of the PVDF-based SAW sensor model in the time domain is implemented. The impulse signal (in Figure 4.4) is a one-cycle 2.5 MHz sinusoidal signal with a magnitude of 1 V and lasts 18 cycles (7.2 μs) in total.

This signal is applied to the electrodes and busbar at the positive side and the other side is grounded. Figure 4.5 exhibit different views of the transient animation at two critical time points with a scale factor of 10^7. A simplified model is used here to present the wave deformation better. It is clearly seen from Figure 4.5(a) that a set of SAWs with

three-wavelength are mainly generated by the three input IDT pairs, which is consistent with the one-cycle impulse excitation. Other wave modes such as P-wave and S-wave can be slightly captured in front of the SAWs traveling a little bit quicker. A significant drawback of the single-finger IDT is the triple transit interferences that are due to the multiple wave reflections between the electrodes, which are shown in Figure 4.5(a) traveling behind the main SAWs.

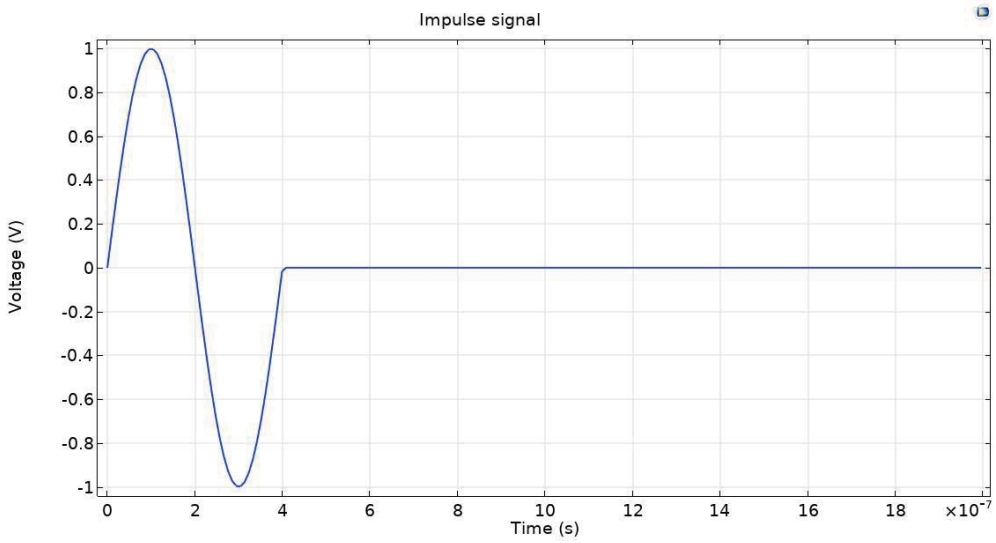

Figure 4.4 A 2.5 MHz impulse sinusoidal signal lasting 7.2 μs (partially presented in the plot from t=0 to 2 μs).

A continuing fluctuation of the input IDT is noted, which is mostly caused by a large number of wave reflections between the electrodes and its inertia due to the impulse excitation. However, even those reflections and inertia are existing, the large displacement of the IDT after the excitation stopped is still not ideal. Hence, further analysis with more precise meshed sized is recommended.

In Figure 4.5(b), after encountering the output IDT as shown, portion of the SAWs are reflected back, while the main portion of them transfer their mechanical energy to the

electrical energy. Figure 4.5 (c) and (d) present the cross-section view at the center of the substrate along the x-axis. The generated waves are purely propagated near the top surface of the substrate which validates with the working principle of the SAW sensor.

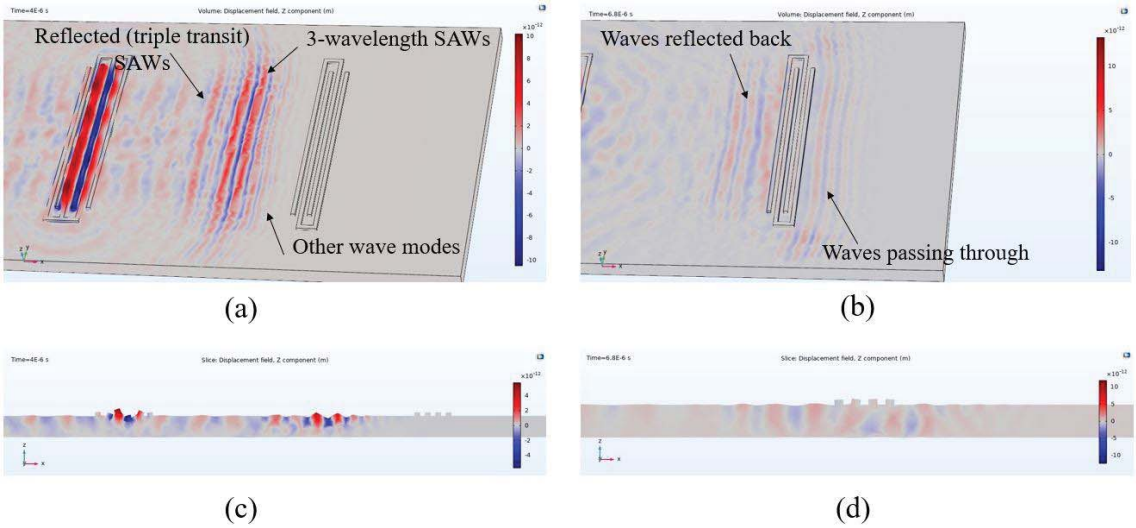

Figure 4.5 Leading and cross-section views of the SAW sensor at the time of a), c) t=4 μs and b), d) t= 6.8 μs.

Same as the input IDT, one side of the output IDT is grounded, and another side is regarded as the positive terminal where the receiving voltage is obtained. An electrical signal vs. time plot is extracted from the COMSOL solution (Figure 4.6). The blue and green curves represent the transmitting and receiving voltage signals, respectively. Three prominent peaks are acquired from the receiving signal that refers to the three-wavelength SAWs. The width of the receiving wavelength shows good consistency with the wavelength of the input signal.

Using the data of the receiving signal, the Rayleigh wave velocity of the PVDF substrate can be calculated as the quotient of the delay line length and time delay, whose result is approximately equal to 770 m/s. With the material properties of PVDF, a

theoretical estimate of 755 m/s can also be computed by using Equation 2.8 and 2.9, which nearly matches the result with the COMSOL solution. This velocity is essential for evaluating the device frequency response. Based on the confirmed wave velocity, the center frequency can be calculated by Equation 2.10, which is supposed to be near 2.55 MHz.

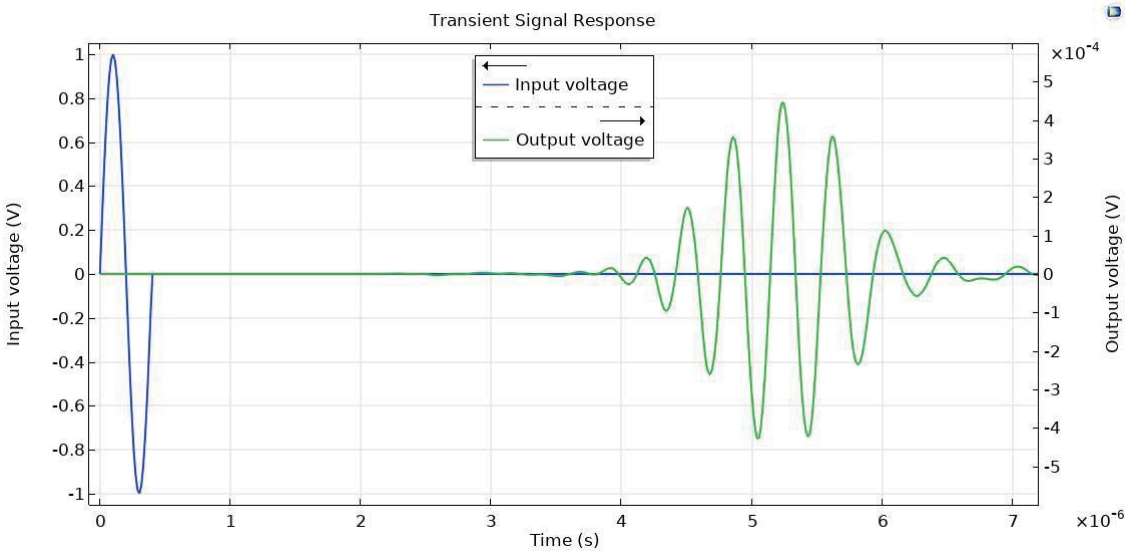

Figure 4.6 Signal response from the transient analysis.

4.4. Frequency Domain Analysis

In order to evaluate the frequency-based parameters, such as S-parameters and Y-parameters, a "Terminal" feature in the physics options of COMSOL is used. Within the four Terminal types (Charge, Voltage, Circuit and Terminated), the Terminated type connects the aimed terminal to a characteristic impedance that represents the extrinsic transmission line (Multiphysics, 2013), where the S-parameters are automatically computed no matter how many terminals there are. This impedance can be manually set and is often assumed to be 50 ohms. The Terminated requires an input power $P_{0,}$ which

works similarly to a vector network analyzer (VNA). Instead of using 1 V voltage as input, a P_0=0.01 W is adopted based on the VNA used for the experimental measurement, whose input power is 1 dBm.

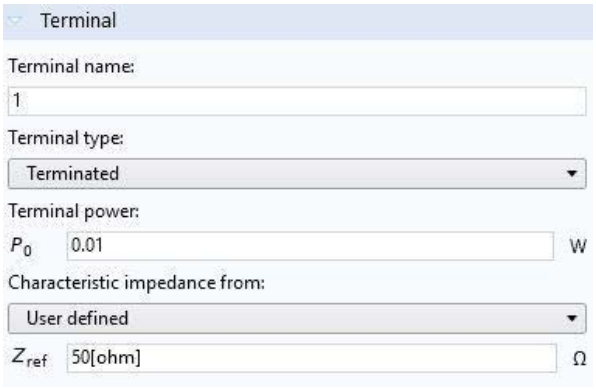

Figure 4.7 Terminal setting with a 0.01 W input power and 50 Ω characterized impedance.

In Figure 4.8, the S_{11} and S_{21} (insertion loss) parameters in dB obtained from both the COMSOL and COM-based MATLAB analyses are presented and compared. From the COMSOL results, the center frequency is near 2.5 MHz, which matches the initial guess. The bandwidth is close to 1.6 MHz, in which the same result can be obtained by the theoretical computation using Equation 2.14. Some ripples are observed within the passband that may be caused by several second-order effects mentioned in the previous chapter. The MATLAB algorithm is initially assuming the SAW velocity on the metallized sections the same as the velocity on free sections. It has been demonstrated that the larger velocity variation can leads to severer ripples by changing this variation in the MATLAB algorithm, which is not shown here. So, the COMSOL solution is more realistic and reliable compared to the theoretical results.

The constants needed for the MATLAB algorithm of PVDF are listed in Table 4.2. The MATLAB result shows a similar trend and magnitude of *IL* in the main lobe with the

COMSOL solution. Hence, the results confirm the reliability of both approaches. Compared to COMSOL simulation, the MATLAB algorithm does not consider the complex BCs as shown in Figure 4.2, and the specific configuration of the SAW sensor, whose result is not as practical as COMSOL.

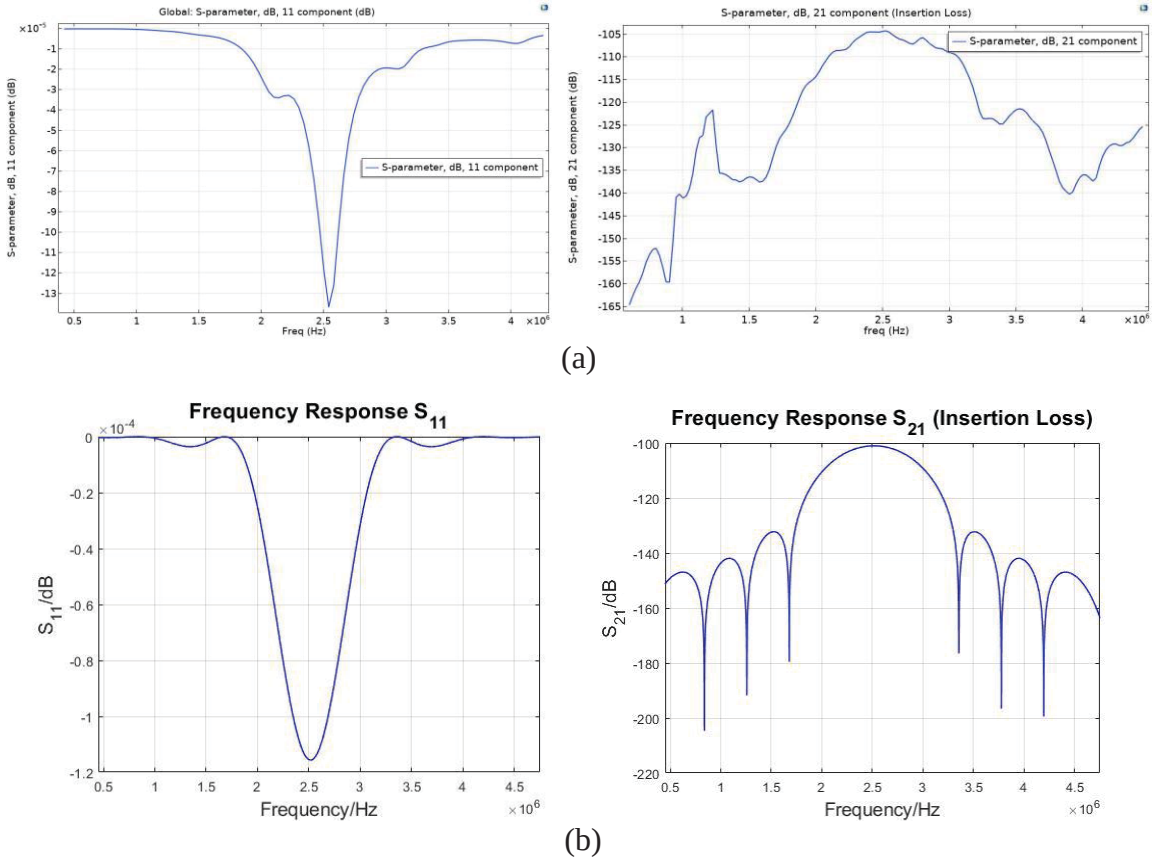

Figure 4.8 S_{11} and S_{21} responses evaluated by a) COMSOL and b) MATLAB.

It is noticed from the *IL* curve (Figure 4.8) that the PVDF-based SAW sensor performs a huge insertion loss, which is more than -100 dB at the center frequency. And the S_{11} is not able to reach -10 dB, under which, the quality of signal transmitting is acceptable. This is mainly because of the low electromechanical coupling factor k^2 of

PVDF. In the next section, an analysis of a $LiNbO_3$-based SAW sensor with higher k^2 and larger stiffness is introduced.

Table 4.3

Material properties of the $LiNbO_3$ substrate (Comsol, 2007).

Material	**Description [unit]**	**Value**
Lithium niobate ($LiNbO_3$)	Density ρ $[kg/m^3]$	4,700
	Elastic stiffness matrix c^E $[10^{10} \cdot Pa]$	$\begin{bmatrix} 20.29 & 5.292 & 7.491 & 0 & 0 & 0 \\ 5.292 & 20.29 & 7.491 & 0 & 0 & 0 \\ 7.491 & 7.491 & 24.31 & 0 & 0 & 0 \\ 0 & 0 & 0 & 5.990 & 0 & 0 \\ 0 & 0 & 0 & 0 & 5.990 & 0 \\ 0 & 0 & 0 & 0 & 0 & 7.488 \end{bmatrix}$
	Piezoelectric-stress matrix e $[C/m^2]$	$\begin{bmatrix} 0 & 0 & 0 & 0 & 3.695 & -2.534 \\ -2.538 & 2.538 & 0 & 3.695 & 0 & 0 \\ 0.1936 & 0.1936 & 1.309 & 0 & 0 & 0 \end{bmatrix}$
	Relative permittivity matrix ε_r^S	$\begin{bmatrix} 43.6 & 0 & 0 \\ 0 & 43.6 & 0 \\ 0 & 0 & 29.16 \end{bmatrix}$
	Curie temperature T_c $[°C]$	1,157
	Electromechanical coupling factor k^2	0.65

4.5. Comparison between the PVDF and $LiNbO_3$-based Sensors

$LiNbO_3$ (Lithium Niobate) is an artificial material whose single-crystal performs outstanding dielectric properties and is frequently used to fabricate the SAW substrate (Yamada, Niizeki, & Toyoda, 1967). The critical material properties of $LiNbO_3$ required for simulating the SAW sensor model are listed in Table 4.3.

$LiNbO_3$ transmits the SAWs much quicker than the PVDF owing to its higher stiffness-to-density ratio. The Rayleigh wave velocity in the $LiNbO_3$ substrate was

reported to be 3488 m/s by several publications (Adler, 2000; Campbell, 1998; Kannan, 2006; Krishnamurthy, 2007). By plugging the velocity value into Equation 2.10, its theoretical center frequency f_0 is supposed to be near 11.6 MHz.

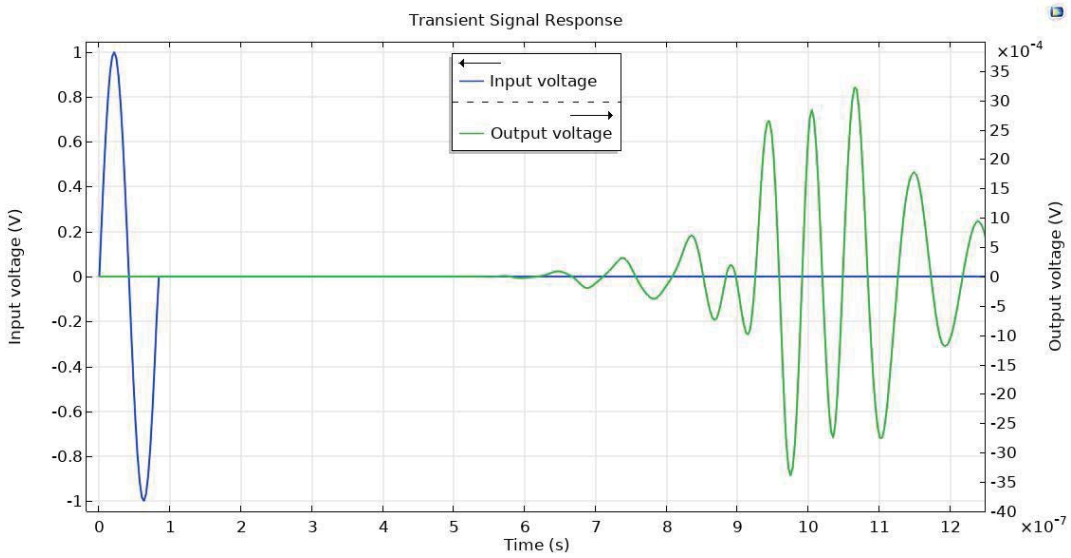

Figure 4.9 Signal response of the $LiNbO_3$-based sensor from the transient analysis.

Transient analysis for the $LiNbO_3$-based SAW sensor model is run firstly. The frequency of the input signal is adjusted to its center frequency, 11.6 MHz, and a new signal response in the time domain is shown in Figure 4.9.

Table 4.4

A comparison of the information obtained from the two signal responses using PVDF and $LiNbO_3$ as substrate.

Description [unit]	**PVDF**	**$LiNbO_3$**
Frequency of the input signal [MHz]	2.5	11.6
Time delay [μs]	4.8	0.94
Maximal amplitude of the output signal [mV]	0.45	3
Electromechanical coupling factor	0.14	0.65

A comparison of the two signal responses using PVDF and $LiNbO_3$ as a substrate can be seen in Table 4.4. The time delay apparently reduces a lot that fits the previous guess. A higher peak magnitude near 3 mV is caught compared to the 0.45 mV of the PVDF-based SAW sensor, demonstrating that a larger k^2 contributes to a bigger magnitude of signal response, hence better transmitting quality.

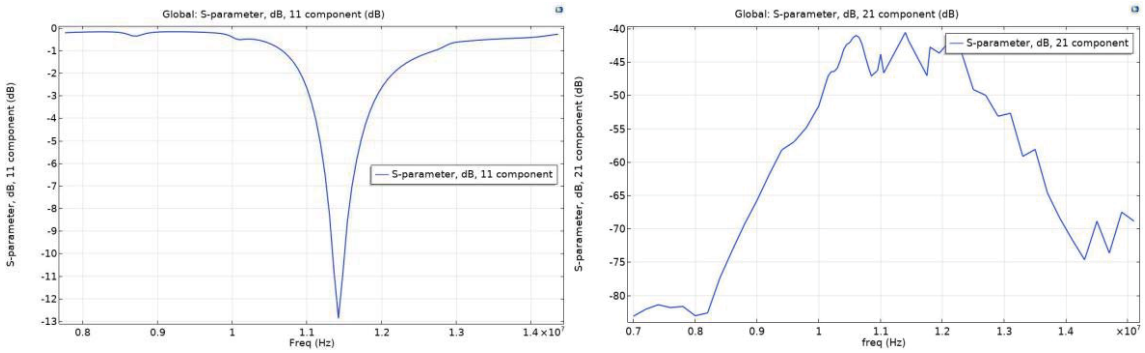

Figure 4.10 S_{11} and S_{21} responses of a $LiNbO_3$-based SAW sensor.

Figure 4.10 presents the S_{11} and S_{21} (IL) responses of the $LiNbO_3$-based SAW sensor, in which the center frequency f_0 is captured near 11.4 MHz that nearly matches the theoretical assumption. The little difference between the simulated and assumed center frequency (11.6 MHz) might be due to the mass loading effects of the IDT, in which the thicker electrodes can reduce the value of f_0, vice versa. The improvement of IL is clearly observed compared to the PVDF-based SAW sensor; whose magnitude reaches -40 dB. The S_{11} value at center frequency also extends beyond -10 dB, which shows a better signal transmission condition. Also, a more precise mesh size is recommended for the COMSOL simulation to reduce the noises in the frequency responses.

4.6. Summary

The chapter brings out a set of numerical analyses of the designed SAW sensor in detail using the COMSOL Multiphysics. The results from both time and frequency domains are presented, which show good consistency with the theoretical assumptions and are well-validated by the COM-based MATLAB solutions. A comparison between the PVDF and $LiNbO_3$-based SAW sensors is performed, which indicates the stiffer materials have the potential for higher center frequency due to their larger wave velocity. It has also been proved that the material with a higher electromechanical coupling factor has better response quality with much lower losses of power.

5. Sensing Mechanism and Calibration

In this chapter, the sensing mechanisms of the SAW sensor for different measurands are explored to demonstrate its multi-functional sensing ability. The strain and temperature are the two typical phenomena within the mechanical and thermal domains, which are chosen as the measurands for numerical analysis in this chapter. The SAW sensor is calibrated by establishing the functional correlations between the variations of frequency response and the measurand levels. Some factors that may influence the sensing effects are discussed.

5.1. Mechanism and Measurand

From the previous chapters, the designed SAW sensor is tested through both theoretical and numerical analyses. The signal responses in time and frequency domains are evaluated with high quality and veracity. As the next step, the sensing mechanism of the SAW-DL sensor is essential for performing the sensing ability, which needs to be further explored.

As briefly mentioned in Chapter 2, the basic mechanism underlying the sensor is its sensitivity to the ambient perturbations caused by the external phenomena. These perturbations are firstly captured by the propagating SAWs that contribute to variations in the wave characteristics. A typical and visualized physical property to represent the variation is the SAW velocity, whose changes can be expressed by the partial effects of multiple factors (Ricco, Martin, & Zipperian, 1985):

$$\frac{\Delta v}{v_0} = \frac{1}{v_0}\left(\frac{\partial v}{\partial \varepsilon}\Delta\varepsilon + \frac{\partial v}{\partial T}\Delta T + \frac{\partial v}{\partial \sigma}\Delta\sigma + \frac{\partial v}{\partial m}\Delta m + \frac{\partial v}{\partial H}\Delta H + \cdots\right) = \kappa\frac{\Delta f}{f} \qquad (5.1)$$

where v_0 is the unperturbed wave velocity, and κ is a coefficient relating the velocity variations and frequency shifts. As Equation 5.1 says, all of these factors, mechanical strain ε, temperature T, conductivity σ, mass loading m, and humidity H, can produce the impacts on the wave velocity simultaneously, as well as the overall wave characteristics.

It needs to be noticed that one cannot only monitor the single measurand without considering others' interference. Either the multiple reference sensor or certain compensations should be implemented in the sensing environment, and the whole sensing system should be enhanced to possess enough selectivity and sensitivity dedicated to the aimed measurand.

Once the SAWs encounter the output IDT, the variations are then acquired and measured through the frequency response and postprocessing procedure. A dimensionless fractional frequency shift f_s for representing these changes in frequency responses is expressed in *ppm* as (Ricco et al., 1985):

$$f_s = \frac{\Delta f}{f} = \frac{f' - f_0}{f_0} \times 10^6 \; ppm \tag{5.2}$$

A connection between the frequency shift and the targeted measurand level is required to establish the functional correlation for sensor calibrations. The relative sensitivity of a SAW sensor S_{SAW} can be characterized as the ratio of the absolute fractional frequency shift f_s to the change of the measurand levels $\Delta\alpha$ as:

$$S_{SAW} = \frac{|f_s|}{\Delta\alpha} \tag{5.3}$$

In a general experimental testing, a series of subcases under different levels of targeted measurand are examined. The frequency shift of each subcase is extracted and

collected as a set of discrete data points that are plotted in an x-y graph. An example diagram is shown in Figure 5.1. The functional correlation can be built to find the calibration based on the plot's tendency, and the sensor sensitivity is equal to the slope of the curve. The more data points the experiment setup tests, the more accurate the result is.

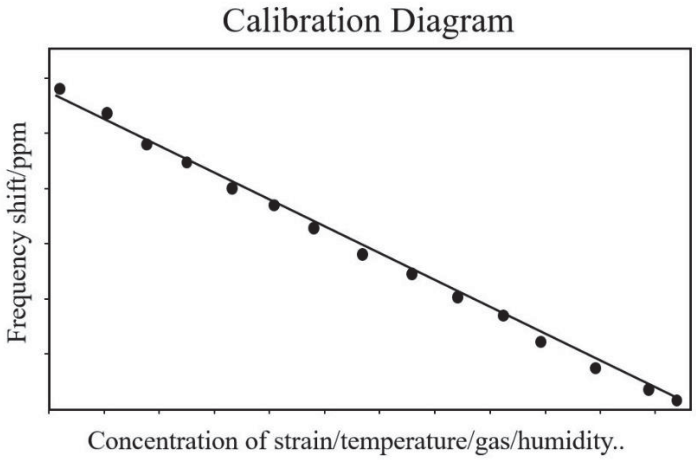

Figure 5.1 Example of a calibration diagram with a linear trendline.

Instead of conducting the real experimental setup, the thesis uses the COMSOL Multiphysics with a well-defined testing environment to simulate and confirm the sensing ability of the designed SAW-DL sensor.

5.2. Strain Measurement

In engineering structures, evaluation of strain concentration due to various loads such as aerodynamic, thermal, and defects, necessitates a monitoring system that can provide beneficial real-time information to avoid catastrophic failures. Due to its special sensing mechanism, the SAW-DL sensor shows excellent ability and potential for strain measurement against the conventional strain sensors, which are not suitable for high-

frequency conditions and wireless sensing in harsh environments and inaccessible locations.

5.2.1. Model Setup

SAW sensor can directly sense the external strain and transfer the information by its piezoelectric substrate. In order to maximize the effect of strain, the material selection for the SAW strain sensor requires to be taken into more consideration. As a typical piezoelectric polymer, PVDF is chosen due to its high flexibility and low stiffness, which makes it able to perfectly absorb the external strain without leaving a massive negative impact on the host structure. The elastic and piezoelectric properties of PVDF can be found in Table 4.2.

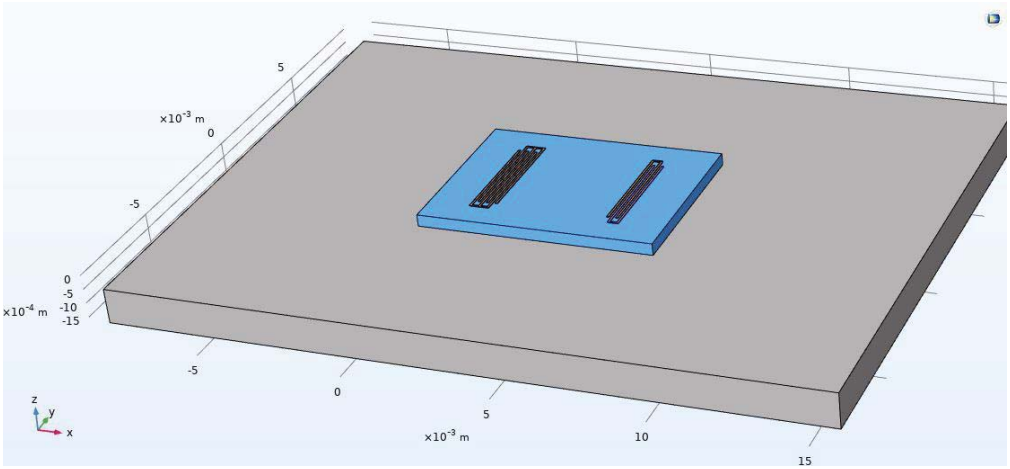

Figure 5.2 Schematic of a cuboid Al base setup with the left boundary fixed.

A cuboid base setup is built to simulate the strain testing environment, shown in Figure 5.2. The cuboid base is regarded as the host structure for the PVDF-based SAW sensor whose material is assigned as Aluminum 6063 from the COMSOL material database. The SAW-DL sensor is bonded to the top of the base. Generally, a mismatch at the bonding polymer adhesive is inevitable, which may decrease the sensitivity. In this

case, since the chosen material, PVDF, doesn't perform a large difference in stiffness with the bonding adhesive, this mismatch is assumed to be neglected.

Different from the analysis types used in the previous chapter, the testing setup is normally subjected to both static and harmonic loads. The strain, as well as other ambient phenomena, is counted as the static load, while the input signal is the harmonic load. The static load case can distinctly affect the frequency responses of the structure; therefore, a proper simulation approach is well needed for the case. In COMSOL, the "Prestressed analysis" is introduced to solve this static-harmonic-combined problem.

Nevertheless, the "Terminal" feature used before for evaluating the S-parameters is not available in this analysis type. The "RMS (root mean square) Displacement" solution is used to replace the S_{21} parameter, which shows even smoother and clearer results due to its particular expression based on the RMS operation. The solutions from the S_{21} parameter and RMS displacement may not have the exact same curve tendencies, but they perform the same center frequency; hence this substitution is tolerable. The target object for outputting the RMS displacement can be a point or an integral area. In this case, a point is picked in the model at the bottom center of the first output finger.

The mechanical strain is generally induced by either external force or moment. Instead of implementing these two types of loads that are hard to generate certain wanted strain values, the "Initial stress and strain" feature in COMSOL is used, defining a component domain to bear the desired value of stress or strain along a particular direction at the initial stage. Nevertheless, this feature needs a constraint of additional degrees of freedom (DOF), which can be the fixing of either three unaligned points, an edge plus an off-line point, or a surface boundary.

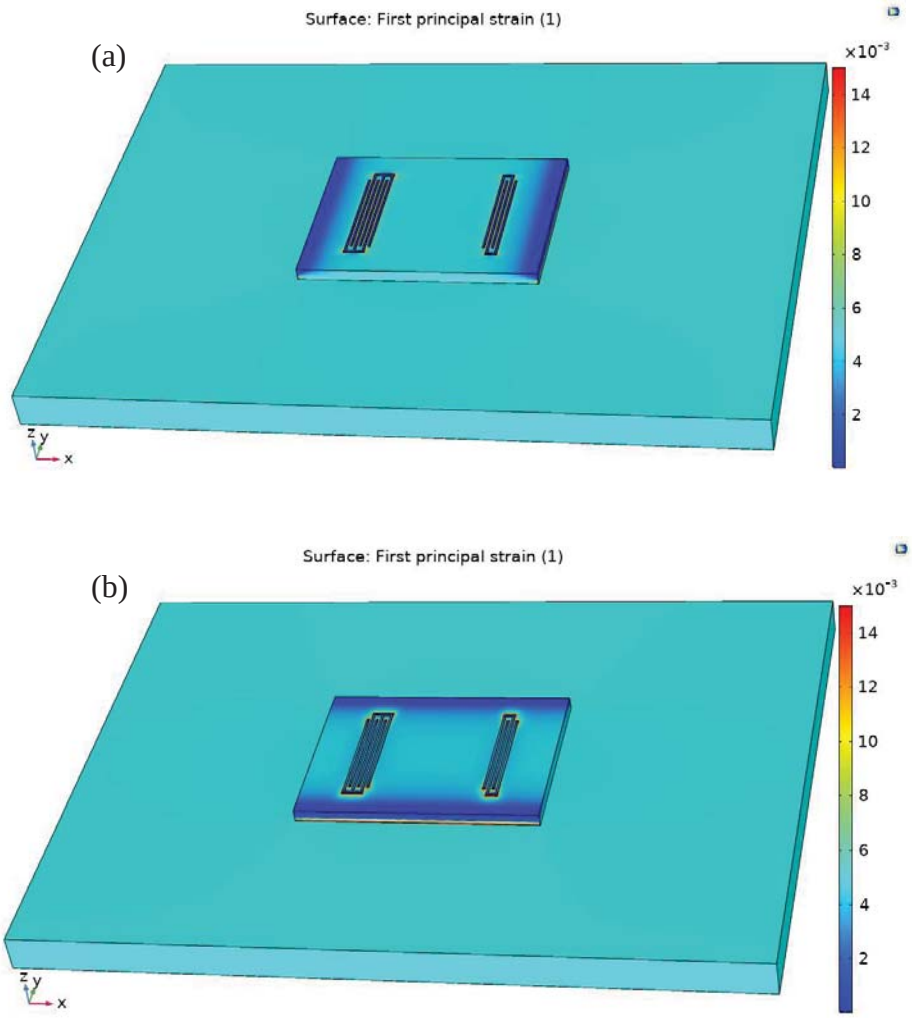

Figure 5.3 Strain distributions of the model setup under a strain level of 0.005 along the direction a) parallel and b) perpendicular to the x-axis.

In real-life applications, the strain may occur along any casual direction in the host structure. This model setup is not going to consider all but the directions that are parallel and perpendicular to the IDT orientation (x-axis). For the parallel case, the left side of the Al base is fixed to fulfill the requirements of the Initial strain setting; similarly, the backside of the base is fixed for the perpendicular case. Figure 5.3 performs the 3D solution plots of the stationary analyses for both cases with the original scale, in which

the strain value is set to be 0.005. The legends at the right size are describing the magnitudes of the first principal strain.

In both Figure 5.3 (a) and (b), the color near the strain level of 0.005 is uniform distributed throughout the Al base, which means the host structure is well deformed under the desired strain level. The major body of the sensor for the parallel case has the same strain magnitude of 0.005 as the base; thus, the SAWs are able to adequately catch the strain information while propagating through the delay line region. It's also noticed that some large strains occur at the bonding corners between the base and substrate, and the IDT and substrate, which may also affect the frequency response. The perpendicular case exhibits similar results, whereas it performs the transverse stretch instead of the longitudinal.

5.2.2. Strain Measurement Result and Discussion

A series of strain levels with an incremental step of 0.0025 are applied to the Al base for testing. Figure 5.4 presents the testing result in both cases. The magnitude decaying with the increasing of strain can be noticed in both cases, which fits the fact that the external strain can lead to additional losses of signal power. For the parallel case, the center frequencies shift to the left direction as the strain level rises, whereas the perpendicular case shows the opposite trend with smaller variations in frequency shifts.

From Equation 2.10 ($f_0=v_R/\lambda$), it is known that the frequency shifts in a SAW strain sensor are determined by a combination of the changes in the IDT geometry and SAW velocity. For the parallel case, the IDT electrodes are stretched towards the IDT orientation, which enlarges the SAW wavelength. And due to the pre-applied strains, the substrate tends to be stiffener than before, inducing a lightly larger SAW velocity. The

results show that the IDT geometry changes dominate the shifts of the center frequency for the parallel case; however, the SAW velocity is the only reason case that contributes to the increasing of the center frequency for the perpendicular since the SAW wavelength does not alter.

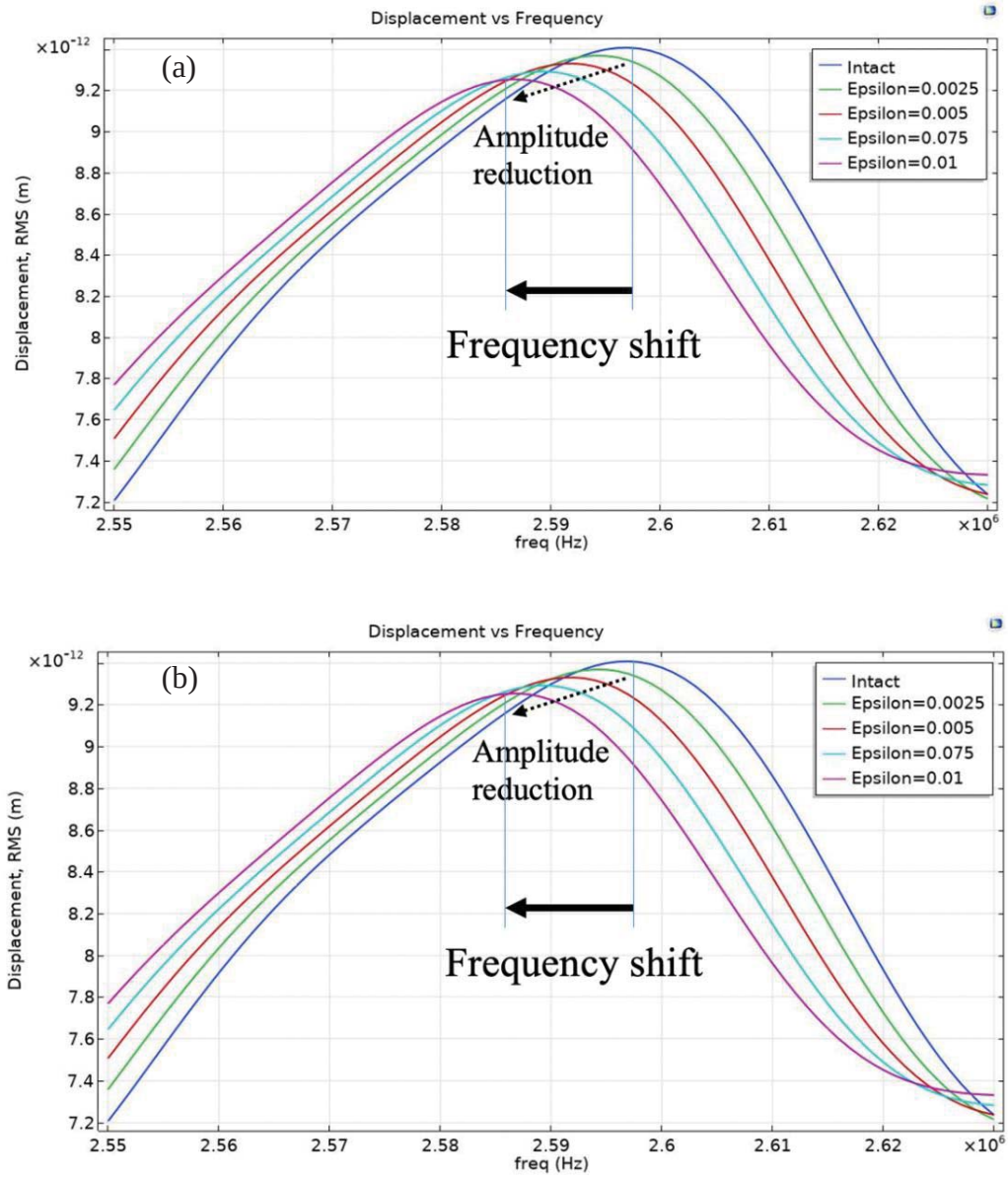

Figure 5.4 Frequency shifts of a) parallel and b) perpendicular cases.

Correlating the dimensional frequency shifts vs. the corresponding strain concentrations, a calibration diagram is made (Figure 5.5), in which both curves present good linearity and low errors. The sensitivities of the SAW sensor for the two cases are calculated to be 0.4083 *ppm/με* and 0.3405 *ppm/με*, respectively, where *με* is the dimensionless unit of micro-strain.

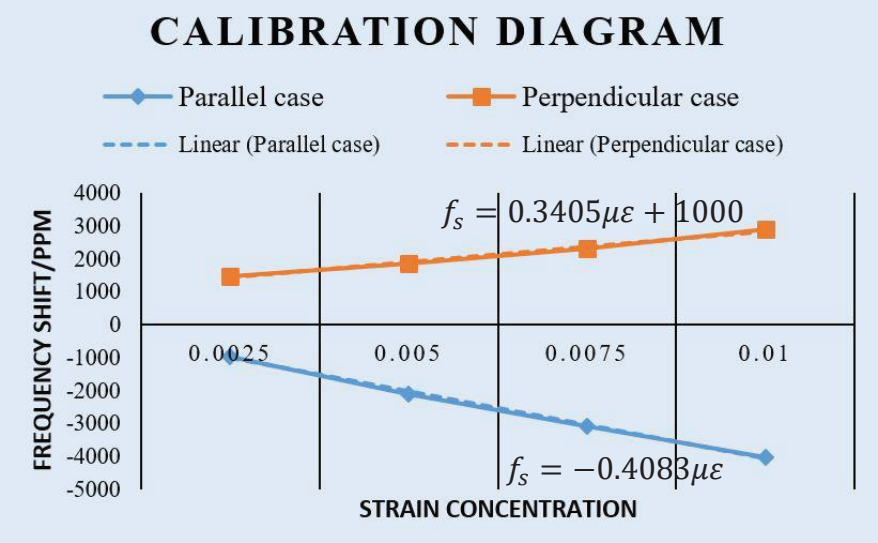

Figure 5.5 Calibration diagrams of both parallel and perpendicular cases supplemented with linear trendlines.

5.3. Temperature Measurement

The high demands for excellent temperature monitoring systems are attributable to the interminable over-heating accidents occurring on a variety of engineering components and parts such as engines, connectors, and other power equipment. The irregular rising of operating temperature can easily cause the failure, aging, or overload of the structure, which must be perceived at the very beginning to avoid tragic damage. The SAW sensor is found to have good sensitivity to temperature change and has collected great interest within this field.

The sensing mechanism of the SAW-DL temperature sensor is relatively similar to its strain sensor. Instead of obtaining the strain information directly, the SAW sensor may either change its material properties or dimensions under the influence of high temperature, which results in the variation in the SAW characteristics.

5.3.1. Model Setup

Due to the high-temperature sensing condition, a compromise for the material selection needs to be made between several factors: high Curie temperature, large electromechanical coupling factor, and low stiffness. Compared to PVDF, which has a low Curie temperature, $LiNbO_3$ is more suitable for the high-temperature operating environment, which is chosen as the material of the aimed SAW temperature sensor.

Table 5.1

Thermal properties of the $LiNbO_3$-based SAW sensor (Comsol, 2007).

Material	**Description [unit]**	**Value**
Structural Steel	Thermal expansion coefficient α [10^{-6}·1/K]	12.3
	Thermal conductivity k [$W/(m·K)$]	44.5
	Heat capacity Cp [$J/(kg·K)$]	475
Lithium Niobate	Thermal expansion coefficient α [10^{-6}·1/K]	15
	Thermal conductivity k [$W/(m·K)$]	4.6
	Heat capacity Cp [$J/(kg·K)$]	648

To solve the thermal-related problems in COMSOL, the “Heat transfer in solid” interface, as well as the Multiphysics coupling of “Thermal expansion”, is added that runs together with the piezoelectricity interface. Besides the elastic and piezoelectric properties that have been listed in Table 4.3, the Heat transfer interface also requires

critical thermal properties of the materials for both IDT and substrate, which is presented in Table 5.1.

The model setup and its boundary conditions remain the same as the strain case (referring to Figure 5.2). Using the “Temperature” feature inside the Heat transfer interface, the desired temperature levels are assigned to each boundary of the whole model. Figure 5.6 presents the 3D solution plot of the Von Mises stress distributions under the temperature level of 350 *K*.

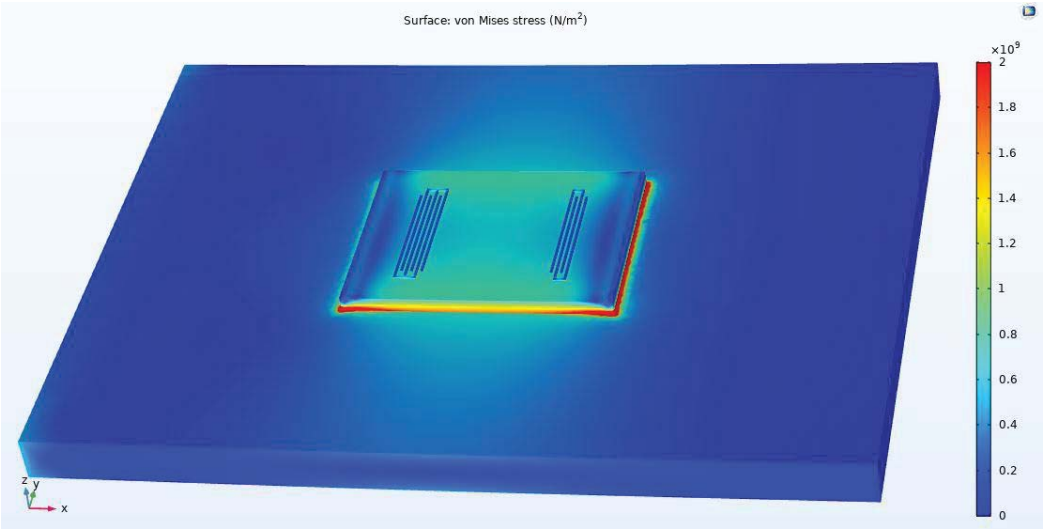

Figure 5.6 Von Mises stress distribution of the model setup under the temperature level of 350 *K*.

Due to the effects of temperature, each component tends to expand itself. The component with a larger thermal expansion coefficient is attempting to swell up over others, leading to some high-stress parts. The delay line region is well under stress compared to the sizes of substrate and base, which enables SAWs to sense the temperature impacts sufficiently.

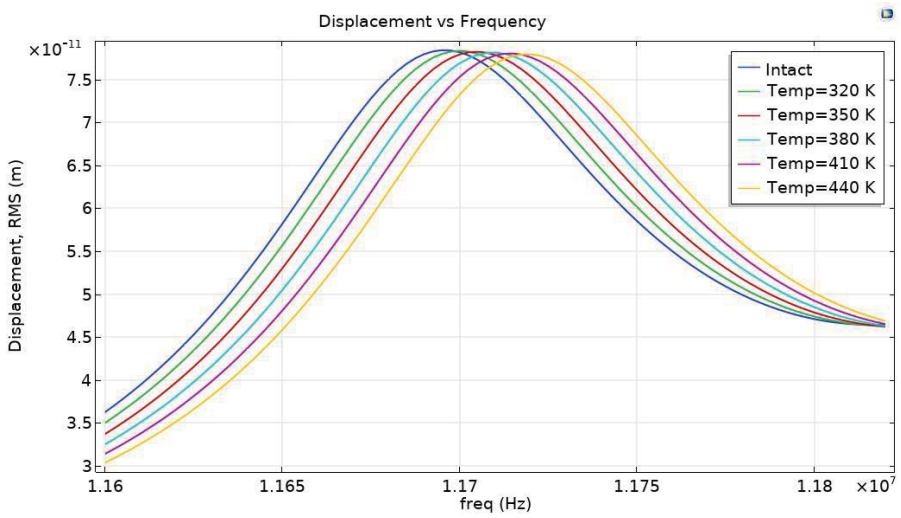

Figure 5.7 Frequency shifts of the SAW temperature sensor under linear levels of temperature conditions with an incremental step of 30 *K* and an intact (reference) temperature of 293.15 *K*.

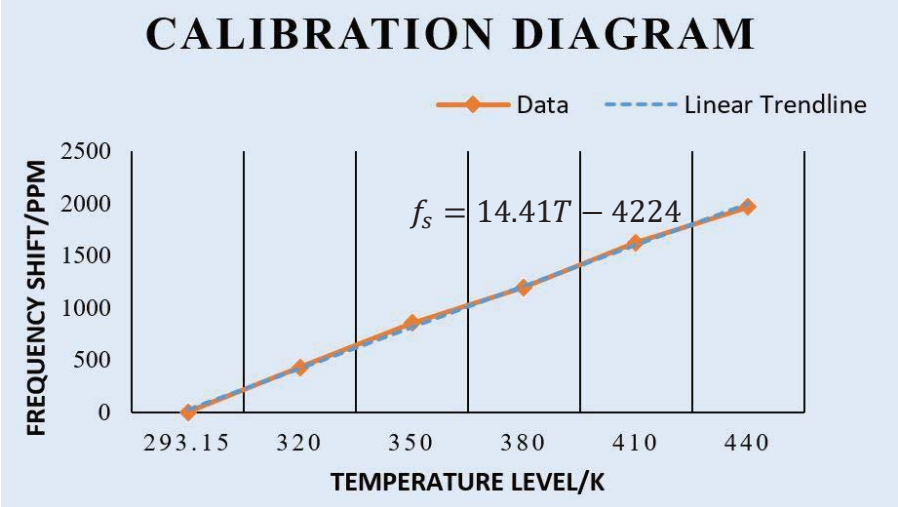

Figure 5.8 Calibration diagram of the SAW temperature sensor with a linear trendline.

5.3.2. Temperature Measurement Result

Maintaining the geometry of the model setup, a series of temperature levels with an incremental step of 30 *K* are applied to the whole model for testing. An intact condition is set under the temperature of 293.15 *K* (20 ℃) as the reference case. Figure 5.7 and 5.8 show the testing result and calibration diagram, in which the frequency shifts keep good

linearity. The calculated sensitivity of this temperature sensor is 14.41 *ppm/K*, which is acceptable.

5.3.3. Sensing Layer

The sensing layer of a two-port SAW-DL sensor refers to a sensitive film that is coated within the delay line region for exposure to ambient phenomena (Figure 5.9). It is required to provide extraordinary selectivity and sufficient sensitivity to the target measurand, which helps the senor to have better detection.

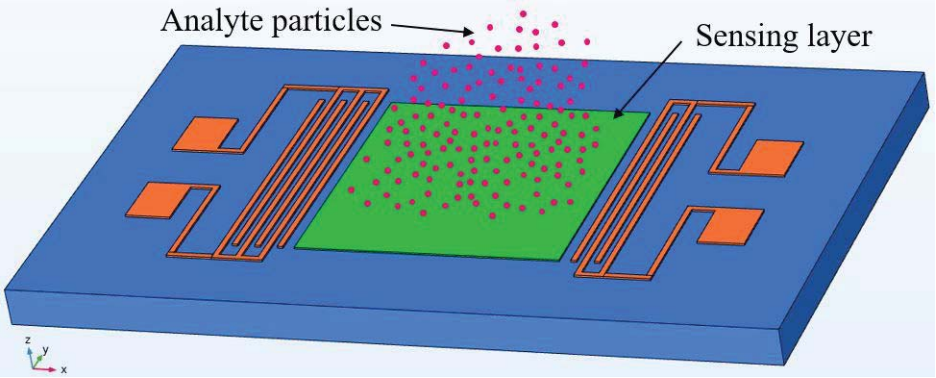

Figure 5.9 Schematic of a sensing layer coated on a two-port SAW-DL sensor.

The sensing layer might not be needed for the strain measurement since the mechanical strain can be detected directly. However, for the analytes such as gas, humidity, and chemicals, either the substrate or IDT doesn't perform sensitivity to these measurands. So, the SAW sensors for these specific sensing cases must be equipped with certain sensing layers. The temperature sensing just falls somewhere in the middle position; no previous researches are done to evaluate the positivity of a temperature sensing layer for a SAW temperature sensor.

The initial idea in this thesis work is to attach a polymer layer with a relatively large thermal expansion coefficient as the sensing layer. When exposed to high-temperature

conditions, it deforms greater than other components of the model, which may cause additional stretches of the substrate. As the temperature increase, the changes can be more evident.

Polyethylene is selected owing to its high thermal expansion coefficient and good elastic stiffness within the polymers, whose elastic and thermal properties are listed in Table 5.2. The dimension of the layer is initially designed to be 3.6×3.5×0.02 *mm* with its center aligned with the center of the delay line region.

Table 5.2

Elastic and thermal properties of the Polyethylene sensing layer (Comsol, 2007).

Material	**Description [unit]**	**Value**
Polyethylene	Density ρ [kg/m^3]	930
	Young's modulus E [GPa]	1
	Poisson's ratio υ	0.3
	Thermal expansion coefficient α [$10^{-6}\cdot 1/K$]	150
	Thermal conductivity k [$W/(m\cdot K)$]	0.38
	Heat capacity Cp [$J/(kg\cdot K)$]	1900

The testing result with the sensing layer is shown in Figure 5.10. It can be seen that the variations of the frequency shifts are increasing compared to the original geometry, and the reductions of the response magnitude are also observed. The sensor sensitivity rises from 14.41 ppm/K to 16.18 ppm/K (Figure 5.11). Therefore, it is proved that the designed temperature sensing layer is able to improve sensitivity. However, some noises are observed in Figure 5.10, which are mainly caused by the mismatch of the center frequency between the polymer sensing layer and the $LiNbO_3$ substrate.

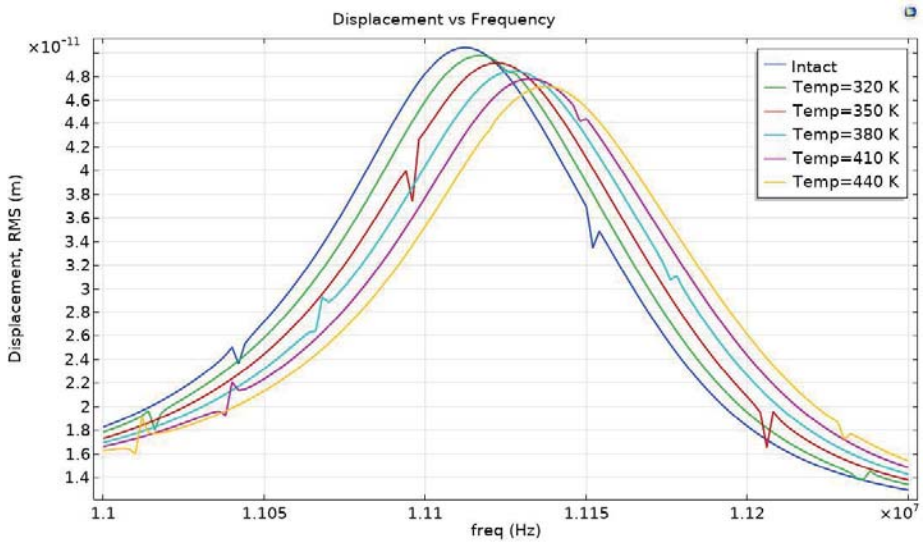

Figure 5.10 Frequency shifts of the SAW temperature sensor with a 3.6×3.5×0.02 *mm* sensing layer.

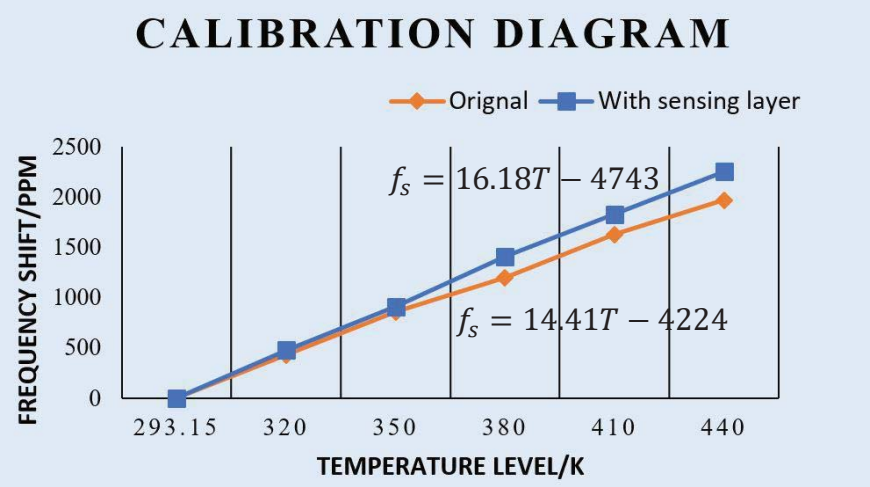

Figure 5.11 Comparison of sensitivities between the SAW sensors without (orange) and with (blue) a sensing layer.

Not limited to the initially designed dimensions and selected material properties, several factors about the sensing layer may affect the sensor's sensitivity. A continuing study focuses on the two main factors about how they influence the frequency responses, which are the thickness and thermal expansion coefficient of the sensing layer.

5.3.3.1 Thickness of the Sensing Layer

The thickness of the sensing layer always matters. A thick sensing layer may result in large interferences shown as the form of noises in the frequency responses. Meanwhile, the thickness needs to maintain upon a certain level to perform sufficient impacts on the sensor.

A parametric sweep of the layer thickness is tested, and the result is shown in Figure 5.12. The sensitivity does increase dramatically when the thickness is relatively higher. However, through the frequency responses of the even larger thickness, the thickness over 25 μm is unacceptable, above which, the frequency responses are just full of noises.

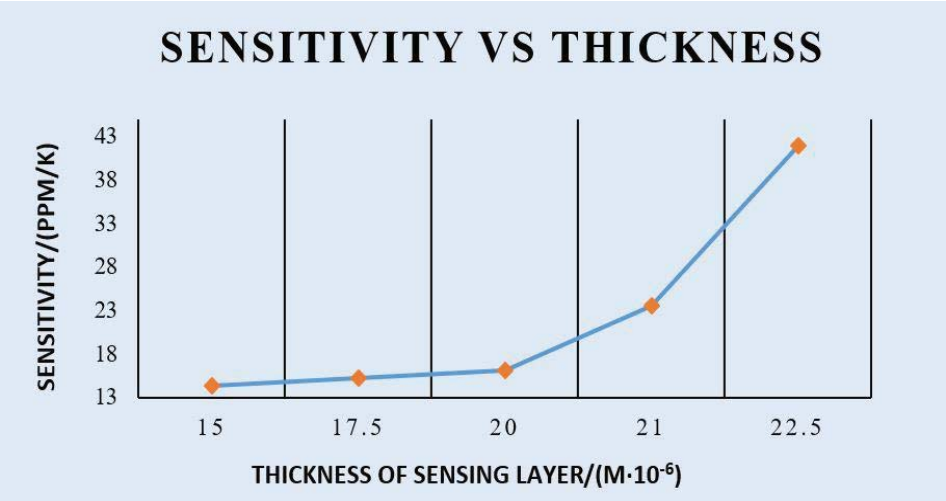

Figure 5.12 The effects of the thickness of a sensing layer on sensor sensitivity.

5.3.3.2 Thermal Expansion Coefficient of the Sensing Layer

In this section, the thermal expansion coefficient is swept as a variable to evaluate its effects on sensor sensitivity. A diagram describing the influences on the sensor's sensitivity due to the thermal expansion coefficient is shown in Figure 5.13. The sensitivity shows the direct proportional relation with the thermal expansion coefficient.

Despite this assumption being too ideal since one cannot only look for the high thermal expansion coefficient without considering their elastic properties when choosing the materials, this idea may provide a direction for designing a better sensing layer.

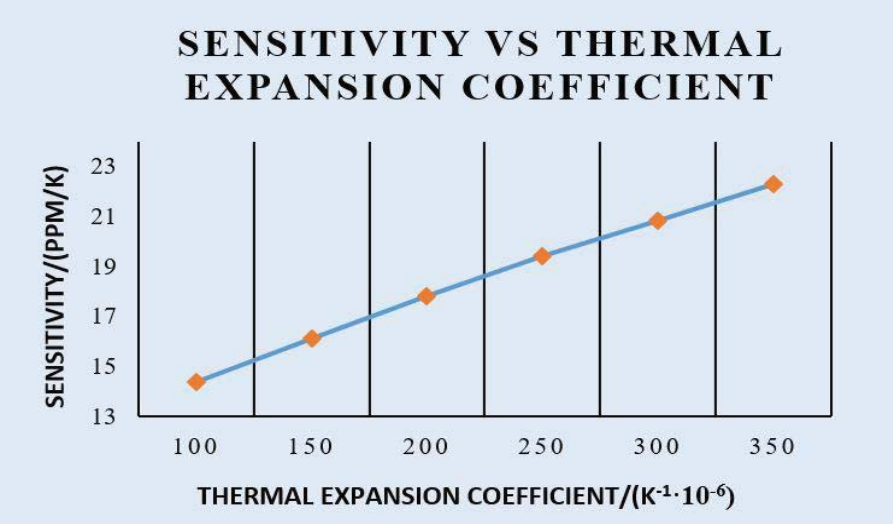

Figure 5.13 The effects of the thermal expansion coefficient of a sensing layer on sensor sensitivity.

5.4. Summary

The chapter is mainly focusing on sensor testing and calibrations in terms of the strain and temperature measurements. For the strain measurement, two typical cases, in which the sensors are strained along the parallel and perpendicular directions, are taken into account and simulated. The sensitivities of both cases are calculated to be 0.4083 *ppm/με* and 0.9399 *ppm/με*, respectively, which are acceptable as a strain sensor. For temperature measurement, a SAW sensor with the original geometry is examined to have a sensitivity of 14.41 *ppm/K*. A temperature sensing layer with dimensions of 3.6×3.5×0.02 *mm* is raised and implemented onto the original SAW sensor. The results demonstrate that the designed sensing layer is able to improve the sensor's sensitivity from 14.41 *ppm/K* to

16.12 *ppm/K*. Two main factors of the sensing layer, the thickness and thermal expansion coefficient, which may affect the sensitivity are also discussed separately. The thicker sensing layer can dramatically increase the sensitivity, whereas the massive noises limit its maximal thickness. The larger thermal expansion coefficient can also contribute to higher sensitivity; however, this parameter is highly material-dependent and hard to alter as desired.

6. Conclusion and Recommendation

The thesis focuses on the theoretical and numerical analyses of a two-port SAW-DL sensor using a COM-based MATLAB algorithm and COMSOL analysis. Both approaches present desired solutions and are well-matched by each other. The results from strain and temperature measurements are acceptable with some principles of a sensing layer summarized. Several recommendations for future work are listed.

6.1. Conclusion

The PVDF and $LiNbO_3$, as two most-widely-used materials for fabricating the SAW substrates, are compared and discussed. The PVDF has a lower electromechanical coupling coefficient but better flexibility, which is suitable as the material for a SAW strain sensor. Meanwhile, the $LiNbO_3$ owns a higher Curie temperature, which can be used for a SAW temperature sensor.

The testing for both the strain and temperature measurements are performed using the COMSOL Multiphysics. The strain testing is operated in two cases, both of which present good linearity in their calibration diagram and great sensitivity. For temperature testing, a temperature sensing layer is designed to study its impacts on the sensor's sensitivity. The results show the sensing layer within the certain material properties and thickness can improve the sensitivity quite much.

6.2. Recommendation

There are several future study directions following this thesis work that can be done to continue the advantages of this numerical analysis approach.

First of all, it's regretful that the thesis isn't able to take advantage of the piezoelectric composites which have the benefits of polymers, single crystals, and ceramics. They are

the better candidates for fabricating the SAW substrate. The main difficulty is that the material properties of them are high depending on the constituents and their proportions, which are challenging to measure and obtain.

Secondly, it is noticed that the frequency shifts are either to the left or right side, meaning the center frequency is affected by different factors in different cases. The reasons for the shift directions are still needed to be studied and verified.

Also, other finger types of the IDT, such as the double-finger and single-phase unidirectional transducer (SPUDT) can be used to get rid of the drawbacks from the single-finger IDT. And optimization of the sensor dimensions and the material selections are also preferred to provide better frequency response with high quality.

Furthermore, the frequency response is generally affected not only by a single measurand, but also other factors simultaneously which are undesirable. Therefore, the compensations need to be done by implementing multiple reference sensors with proper conditions. Continuing with the idea, a multiple sensing network can also be achieved for collecting and summarizing the data information of a large sensing area.

REFERENCES

Abbott, B. (1991). A coupling-of-modes model for SAW transducers with arbitrary reflectivity weighting.

Achour, B., Aloui, N., Fourati, N., Zerrouki, C., & Yaakoubi, N. (2018). *Modelling and simulation of SAW delay line sensors with COMSOL Multiphysics.* Paper presented at the MOL2NET 2018, International Conference on Multidisciplinary Sciences, 4th edition.

Adler, E. L. (2000). Bulk and surface acoustic waves in anisotropic solids. In *Advances In Surface Acoustic Wave Technology, Systems And Applications: Volume 1* (pp. 101-132): World Scientific.

Akdogan, E. K., Allahverdi, M., & Safari, A. (2005). Piezoelectric composites for sensor and actuator applications. *IEEE transactions on ultrasonics, ferroelectrics, and frequency control, 52*(5), 746-775.

Augustine, R., Sarry, F., Kalarikkal, N., Thomas, S., Badie, L., & Rouxel, D. (2016). Surface acoustic wave device with reduced insertion loss by electrospinning p (vdf–trfe)/zno nanocomposites. *Nano-micro letters, 8*(3), 282-290.

Bell, D. T., & Li, R. C. (1976). Surface-acoustic-wave resonators. *Proceedings of the IEEE, 64*(5), 711-721.

Binder, A., Bruckner, G., Schobernig, N., & Schmitt, D. (2013). Wireless surface acoustic wave pressure and temperature sensor with unique identification based on LiNbO3. *IEEE Sensors Journal, 13*(5), 1801-1805. doi:10.1109/JSEN.2013.2241052

Campbell, C. (1998). *Surface Acoustic Wave Devices for Mobile and Wireless Communications, Four-Volume Set*: Academic press.

Chen, D.-P., & Haus, H. A. (1985). Analysis of metal-strip SAW gratings and transducers. *IEEE Transactions on Sonics and ultrasonics, 32*(3), 395-408.

Comsol, A. (2007). COMSOL Multiphysics reference manual. *COMSOL AB*.

Crabb, J., Maines, J., & Ogg, N. (1971). Surface-wave diffraction on LiNbO3. *Electronics Letters, 7*(10), 253-255.

Devkota, J., Ohodnicki, P. R., & Greve, D. W. (2017). SAW sensors for chemical vapors and gases. *Sensors, 17*(4), 801.

Diaz, J., Karrer, H., Kusters, J., Matsinger, J., & Schulz, M. (1975). The temperature coefficient of delay-time for X-propagating acoustic surface-waves on rotated Y-cuts of alpha quartz. *IEEE Transactions on Sonics and ultrasonics, 22*(1), 46-49.

Donohoe, B., Geraghty, D., & O'Donnell, G. E. (2010). Wireless calibration of a surface acoustic wave resonator as a strain sensor. *IEEE Sensors Journal, 11*(4), 1026-1032.

El Gowini, M. M., & Moussa, W. A. (2009). A reduced three dimensional model for SAW sensors using finite element analysis. *Sensors, 9*(12), 9945-9964.

Elsherbini, M., Elkordy, M., & Gomaa, A. (2016). Using COMSOL to model high frequency surface acoustic wave (SAW) device. *Journal of Electrical and Electronics Engineering Research, 8*(1), 1-8.

Freund, L. B. (1998). *Dynamic fracture mechanics*: Cambridge university press.

Haldar, S. K. (2018). Chapter 6 - Exploration Geophysics. In S. K. Haldar (Ed.), *Mineral Exploration (Second Edition)* (pp. 103-122): Elsevier.

Hartemann, P., & Dieulesaint, E. (1969). Intrinsic compensation of sidelobes in a dispersive acoustic delay line. *Electronics Letters, 5*(10), 219-220.

Hartmann, C. S., Bell, D. T., & Rosenfeld, R. C. (1973). Impulse model design of acoustic surface-wave filters. *IEEE Transactions on Microwave Theory and Techniques, 21*(4), 162-175.

Hohmann, S., Kögel, S., Brunner, Y., Schmieg, B., Ewald, C., Kirschhöfer, F., . . . Länge, K. (2015). Surface acoustic wave (SAW) resonators for monitoring conditioning film formation. *Sensors, 15*(5), 11873-11888.

Hu, W. (2011). Experimental search for high Curie temperature piezoelectric ceramics with combinatorial approaches.

Humphries, J., Figuroa, J., Gallagher, M., Gallagher, D., Weeks, A., & Malocha, D. (2016). Interrogating Passive Wireless SAW Sensors with the USRP. *Ettus Research*.

Ji, X., Fan, Y., Qi, H., Chen, J., Han, T., & Cai, P. (2014). A wireless demodulation system for passive surface acoustic wave torque sensor. *Review of Scientific Instruments, 85*(12), 125001.

Jones, S. (2010). *Ground vibration from underground railways: how simplifying assumptions limit prediction accuracy*. University of Cambridge,

Kannan, T. (2006). *Finite element analysis of surface acoustic wave resonators.*

Kharusi, M. S., & Farnell, G. (1970). *Diffraction and beam steering for surface-wave comb structures on anisotropic substrates*. Retrieved from

Krishnamurthy, S. (2007). Wireless Passive Surface Acoustic Wave (SAW) Sensing System.

Länge, K., Rapp, B. E., & Rapp, M. (2008). Surface acoustic wave biosensors: a review. *Analytical and bioanalytical chemistry, 391*(5), 1509-1519.

Malocha, D., Puccio, D., & Gallagher, D. (2004). *Orthogonal frequency coding for SAW device applications.* Paper presented at the IEEE Ultrasonics Symposium, 2004.

Meitzler, A., Tiersten, H., Warner, A., Berlincourt, D., Couqin, G., & Welsh III, F. (1988). IEEE standard on piezoelectricity. In: Society.

Morgan, D. P. (1996). Cascading formulas for identical transducer P-matrices. *IEEE transactions on ultrasonics, ferroelectrics, and frequency control, 43*(5), 985-987.

Multiphysics, C. (2008). Structural Mechanics Module. In: Reference Guide, Vers.

Multiphysics, C. (2013). AC/DC Module user's guide. *New York: COMSOL Multiphysics*.

Rathod, V. T. (2019). A review of electric impedance matching techniques for piezoelectric sensors, actuators and transducers. *Electronics, 8*(2), 169.

Rayleigh, L. (1885). On waves propagated along the plane surface of an elastic solid. *Proceedings of the London mathematical Society, 1*(1), 4-11.

Reindl, L., Shrena, I., Kenshil, S., & Peter, R. (2003). *Wireless measurement of temperature using surface acoustic waves sensors.* Paper presented at the IEEE International Frequency Control Symposium and PDA Exhibition Jointly with the 17th European Frequency and Time Forum, 2003. Proceedings of the 2003.

Ricco, A., Martin, S., & Zipperian, T. (1985). Surface acoustic wave gas sensor based on film conductivity changes. *Sensors and Actuators, 8*(4), 319-333.

Ro, R., Tung, H.-Y., & Wu, S.-J. (2004). Design of two-track surface acoustic wave filters with width-controlled reflectors. *Japanese journal of applied physics, 43*(2R), 688.

Sittig, E. K., & Coquin, G. A. (1968). Filters and dispersive delay lines using repetitively mismatched ultrasonic transmission lines. *IEEE Transactions on Sonics and ultrasonics, 15*(2), 111-118.

Smith, W. R., Gerard, H. M., Collins, J. H., Reeder, T. M., & Shaw, H. J. (1969). Analysis of interdigital surface wave transducers by use of an equivalent circuit model. *IEEE Transactions on Microwave Theory and Techniques, 17*(11), 856-864.

Smith, W. R., & Pedler, W. F. (1975). Fundamental-and harmonic-frequency circuit-model analysis of lnterdigital transducers with arbitralry metallization ratios and

polarity sequences. *IEEE Transactions on Microwave Theory and Techniques, 23*(11), 853-864.

Soluch, W. (2000). Scattering matrix approach to one-port SAW resonators. *IEEE transactions on ultrasonics, ferroelectrics, and frequency control, 47*(6), 1615-1618.

Tancrell, R., & Holland, M. (1971). Acoustic surface wave filters. *Proceedings of the IEEE, 59*(3), 393-409.

Tobolka, G. (1979). Mixed matrix representation of SAW transducers. *IEEE Transactions on Sonics and ultrasonics, 26*(6), 426-427.

Uchino, K. (2017). Chapter 1 - The Development of Piezoelectric Materials and the New Perspective. In K. Uchino (Ed.), *Advanced Piezoelectric Materials (Second Edition)* (pp. 1-92): Woodhead Publishing.

White, R., & Voltmer, F. (1965). Direct piezoelectric coupling to surface elastic waves. *Applied physics letters, 7*(12), 314-316.

Wright, P. (1989). *A new generalized modeling of SAW transducers and gratings.* Paper presented at the Proceedings of the 43rd Annual Symposium on Frequency Control.

Yamada, T., Niizeki, N., & Toyoda, H. (1967). Piezoelectric and elastic properties of lithium niobate single crystals. *Japanese journal of applied physics, 6*(2), 151.

APPENDIX A – MATLAB Algorithm

The following MATLAB algorithm is for modeling a PVDF-based two-port SAW-DL sensor based on the COM model and transmission matrix approach (Krishnamurthy, 2007).

```
rho=1780;E=3E9;nu=0.24;G=E/(2*(1+nu)); %Elastic properties of PVDF
v_s=sqrt(G/rho); %Shear wave velocity
v_r=v_s*(0.862+1.14*nu)/(1+nu); %SAW (Rayleigh wave) velocity on the free sections
v_m=v_r; %SAW velocity on the metallized sections is initially assumed to be the same as free sections.
lambda_r=0.3e-3; %SAW wavelength
f0=v_r/lambda_r; %center frequency
Nfp_in=6;Nfp_out=4; %Number of electrodes in the input and output IDTs
C=1.5e-12; %Capacitance per finger pair per unit length
k_2=0.14; %Electromechanical coupling coefficient of PVDF
ws=1/8*lambda_r; %free section 1/4*lambda of a unit
wf=1/4*lambda_r; %metallized section 1/8*lambda of a unit
f_m=v_m/lambda_r; %frequency of metallized section
ap=3.5e-3; %Acoustic aperture
d=4.5e-3; %Length of the delay line (transmission line)
Z=1/(f0*C*ap*k_2); %acoustic impedance for free sections without fingers
Z_m=1/(f_m*C*ap*k_2); %acoustic impedance for the metallized sections with fingers

i=1;
f_min=0.45e6;
f_max=4.75e6;
for f=f_min:1000:f_max
   lambda=v_r/f;
   omega=2*pi*f;
   %Computation of the ABCD matrix for a single finger
   theta_f=2*pi*f*ws/v_r; %acoustic angle in free region
   theta_m=2*pi*f*wf/v_m; %acoustic angle in metallized region
   %Computation of the free region between fingers
   A_f=cos(theta_f);
   B_f=sqrt(-1)*Z*sin(theta_f);
   C_f=sqrt(-1)*sin(theta_f)/Z;
   D_f=cos(theta_f);
   %Computation of the metallized regions under fingers
   A_m=cos(theta_m);
   B_m=sqrt(-1)*Z_m*sin (theta_m);
   C_m=sqrt(-1)*sin(theta_m)/Z_m;
   D_m=cos(theta_m);
   %Cascading matrix for a single finger to calculate 2x2 A_finger matrix
   A_finger =[A_f B_f;C_f D_f]*[A_m B_m;C_m D_m]*[A_f B_f;C_f D_f];
   %Single finger matrix value
   A_se=A_finger(1,1);
   B_se=A_finger(1,2);
   C_se=A_finger(2,1);
   D_se=A_finger(2,2);
   theta_d=2*pi*f*d/v_r;
   theta_e=acos(A_se);
```

```
Ze=B_se/(sqrt(-1)*sin(theta_e));
%transmission matrix for a single finger of the IDT
t11 =0.5*(2*A_se+(B_se/Z)+Z*C_se);
t12 =0.5*(Z*C_se-(B_se/Z));
t13 =((sqrt (-1)*tan(theta_e/2)*(Z^0.5))/(2*Ze))*(-A_se-1-(B_se/Z));
t21=-t12;
t22=conj(t11);
t23=sqrt(-1)*tan(theta_e/2)*(Z^0.5)*(1+A_se-(B_se/Z))/(2*Ze);
t31=2*t13;
t32=-2*t23;
t33=sqrt(-1)*omega*C*ap*0.5+sqrt(-1)*2*(tan(theta_e/2)/Ze)-sqrt(-1)*(sin(theta_e)*…
(tan(theta_e/2)^2))/Ze;
%computing the 2x2 IDT matrix
t1 =[t11 t12;t21 t22]^Nfp_in;
t3 =[t11 t12;t21 t22]^Nfp_out;
t11_in=t1(1,1);
t12_in=t1(1,2);
t21_in=t1(2,1);
t22_in=t1(2,2);
t12_out=t3(1,2);
t11_out=t3(1,1);
t21_out=t3(2,1);
t22_out=t3(2,2);
Bp=[t13;t23]+[t11 t12;t21 t22]*[-t13;-t23];
Cp=[t31 t32]*[t11 t12;t21 t22]+[-t31 -t32];
t_33p=2*t33 +[t31 t32]*[-t13;-t23];
Tp=[t11 t12;t21 t22]^2;
BN_in=[0;0];
CN_in=[0 0];
BN_out=[0;0];
CN_out=[0 0];
t_33_out=(Nfp_out/2)*t_33p ;
t_33_in=(Nfp_in/2)*t_33p ;
%Input IDT
for i1=1:(Nfp_in/2)
   BN_in=BN_in+(Tp^(i1-1))*Bp;
   CN_in=CN_in+Cp*Tp^(i1-1);
   t_33_in=t_33_in+((Nfp_in/2)-i1)*Cp*Tp^(i1-1)*Bp;
end
%Output IDT
for i2=1:(Nfp_out/2)
   BN_out=BN_out+(Tp^(i2-1))*Bp;
   CN_out=CN_out+Cp*Tp^(i2-1);
   t_33_out=t_33_out+((Nfp_out/2)-i2)*Cp*Tp^(i2-1)*Bp;
end

t13_in=BN_in(1,1);
t13_out=BN_out(1,1);
t23_in=BN_in(2,1);
t23_out=BN_out(2,1);
t31_in=CN_in(1,1);
t31_out=CN_out(1,1);
t32_in=CN_in(1,2);
t32_out=CN_out(1,2);
%ABCD matrix of delay path
A_d=cos(theta_d);
```

```
    B_d=sqrt(-1)*Z*sin (theta_d);
    C_d=sqrt(-1)*sin(theta_d)/Z;
    D_d=cos(theta_d);
    %Computation of transmission matrix for delay path
    d11=0.5*(2*A_d+(B_d/Z)+Z*C_d);
    d12=0.5*(Z*C_d-(B_d/Z));
    d21=-d12;
    d22=0.5*(2*A_d-(B_d/Z)-Z*C_d);
    d2=[d11 d12;d21 d22];
    %Substitutions for convenience
    s1=t1*d2*t3;
    s2=t1*d2*[t13_out;t23_out];
    s3=[t31_in t32_in]*d2*t3;
    s4=[t31_in t32_in]*d2*[t13_out;t23_out];
    %computing Y-parameter (Admittance) for the SAW-DL
    y_11(i)=t_33_in-(s3(1,1)*t13_in/s1(1,1));
    y_12(i)=s4(1,1)-(s3(1,1)*s2(1,1)/s1(1,1));
    y_21(i)=-t31_out*t13_in/s1(1,1);
    y_22(i)=t_33_out-(t31_out*s2(1,1)/s1(1,1));
    %Computing S-parameters using the Y-parameters (assuming the input and output reference impedances
are both equal to 50 ohm)
    R1=50;R2=50; %Only real part of the impedance are considered
    %modified S-parameter including source and load impedance
    s_11_m(i)=((1-R1*y_11(i))*(1+R2*y_22(i))+y_12(i)*y_21(i)*R1*R2)/((1+R1*y_11(i))*…
    (1+R2*y_22(i))-y_12(i)*y_21(i)*R1*R2);
    s_21_m(i)=-2*sqrt(R1*R2)*y_12(i)/((1+R1*y_11(i))*(1+R2*y_22(i))-y_12(i)*y_21(i)*R1*R2);
    i=i+1;
end
%Plot the S11 parameter in dB
figure(1);
f=f_min:1000:f_max;
y1=20*log10(abs(s_11_m));
plot(f,y1,'r');
xlim([f_min f_max]);
title('Frequency Response S_{11}','FontSize',16);
xlabel('Frequency/Hz','FontSize',14);
ylabel('S_{11}/dB','FontSize',14)
set(findall(gca,'type','line'),'linewidth',1,'Color','b')
grid on;
%Plot the S21 parameter in dB
figure(2);
f=f_min:1000:f_max;
y1=20*log10(abs(s_21_m));
plot(f,y1,'r');
xlim([f_min f_max]);
title('Frequency Response S_{21} (Insertion Loss)','FontSize',16);
xlabel('Frequency/Hz','FontSize',14);
ylabel('S_{21}/dB','FontSize',14)
set(findall(gca,'type','line'),'linewidth',1,'Color','b')
grid on;
```

APPENDIX B – Principles of the COMSOL Analysis

This appendix lists a few details about the COMSOL setup for the testing model, including the usages of the COMSOL feature and solution trees, inner equations for material properties and boundary conditions, etc.

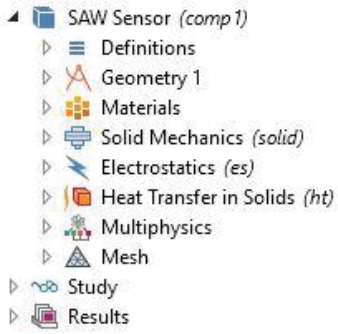

Figure B. 1 Feature tree of a piezoelectric-thermal-combined analysis environment.

Figure B.1 presents the feature tree of a piezoelectric-thermal-combined simulation environment similar to the SAW temperature sensing setup in chapter 5.

The “Solid Mechanics” and “Electrostatics” are the required physics for a piezoelectric analysis, in which the “Solid Mechanics” solves the solid boundary conditions (e.g., fixing, roller) and mechanical loads, while the “Electrostatics” process the electrical boundary conditions (e.g., ground, terminal) and electrical loads. The “Heat Transfer in Solids” can deal with the fundamental thermal problem, such as simulating the solid performance when applying the temperature to certain boundaries.

The “Multiphysics” feature works on the domains where the interactions of different physics occur. The “Study” determines the study types, which can be stationary, frequency, eigenmode, pre-stressed analyses. And the “Results” feature provides a wide range of solution options, as well as diverse plot types.

As discussed in chapter 4, the COMSOL works by following the rules of the partial differential equations (PDEs), which are the basic principles of the scientific phenomena and couplings of multiple physics. Here lists the PDEs behind the corresponding boundary conditions, interfaces, and interactions of multi-physics, which have been used in this thesis work.

The "Fixed constraint" is easy to understand, whose PDE goes

$$\boldsymbol{u} = 0 \tag{B.1}$$

where $\boldsymbol{u}$ is the vector displacement of a single finite element in the target surface, whose direction is parallel to the normal of the element surface. This PDE fits any boundary, even if it's not flat.

The "Low-reflecting boundary condition" used in Figure 4.2 is more complicated. It is mainly intended for letting waves pass out from the model domain without reflection in time-dependent analyses. As a default, the low-reflecting boundary condition takes the material data from the adjacent domain in an attempt to create a perfect impedance match for both pressure waves and shear waves so that

$$\sigma \cdot \boldsymbol{n} = -\rho c_p \left(\frac{\partial \boldsymbol{u}}{\partial t} \cdot \boldsymbol{n}\right)\boldsymbol{n} - \rho c_s \left(\frac{\partial \boldsymbol{u}}{\partial t} \cdot \boldsymbol{t}\right)\boldsymbol{t} = \boldsymbol{d}_i \cdot \frac{\partial \boldsymbol{u}}{\partial t} \tag{B.2}$$

where $\boldsymbol{n}$ and $\boldsymbol{t}$ are the unit normal and tangential vectors at the boundary, respectively, and c_P and c_S are the speeds of the pressure and shear waves in the material. The mechanical impedance $\boldsymbol{d}_i$ is a diagonal matrix available as the user input, and by default, it is set to

$$\boldsymbol{d}_i = \boldsymbol{d}_i(\rho, c_p, c_s) = \rho\left(\frac{c_p + c_s}{2}\right)\boldsymbol{I} \tag{B.3}$$

For the specific study type such as frequency domain analysis, Equation B.2 changes to

$$\sigma \cdot \boldsymbol{n} = -i\omega \boldsymbol{d}_i(\rho, c_p, c_s) \cdot \boldsymbol{u} \tag{B.4}$$

where *i* is the imaginary unit, and ω is the angular frequency.

The "Electrostatics" interface solves for the electric potential *V* using the equation

$$-\nabla \cdot (\varepsilon \nabla V) = \rho \tag{B.5}$$

where ε and ρ represent the permittivity and charge distribution, respectively. The charge usually resides only on surfaces held at fixed potentials. The "Electric Potential", "Ground", and "Terminal" boundary conditions are usually used to fix the potential on the surfaces of a MEMS device.

The PDEs for "Electric Potential" and "Ground" are relatively simple, which are

$$V = V_0 \tag{B.6}$$

$$V = 0 \tag{B.7}$$

The "Terminal" provides a boundary or domain condition for connection to external circuits, to transmission lines, or with a specified voltage or charge. Thus, it has four terminal types, in which the "Terminated" is the only type that is able to calculate the scattering parameters.

In the “Heat Transfer in Solids” interface, “Temperature” and “Thermal insulation” are the two main boundary conditions that are applying the temperature level and preventing the heat flux across the boundary, whose PDEs are

$$T = T_0 \tag{B.8}$$

$$-\boldsymbol{n} \cdot \boldsymbol{q} = 0 \tag{B.9}$$

respectively. $\boldsymbol{n}$ is the normal vector of the boundary, and $\boldsymbol{q}$ is the conductive heat flux vector, which can be calculated by

$$\boldsymbol{q} = k\nabla T \tag{B.10}$$

where k is the thermal conductivity.

The “Multiphysics” feature shown in Figure B.1 explains the interactions between the different physical interfaces. In this case, only two Multiphysics are used: the “Piezoelectric Effect” and “Thermal Expansion”.

The constitutive equations of the piezoelectric effect have been explained in detail in chapter 2. The PDF for “Thermal Expansion” is

$$\varepsilon(\boldsymbol{X}) = \alpha(\boldsymbol{X}, T)\left(T - T_{ref}\right) \tag{B.11}$$

where ε is the thermal strain, and $\boldsymbol{X}$ represents the frame coordinates. α is the secant coefficient of thermal expansion, which can be temperature dependent. T is the temperature level, and the reference temperature T_{ref} can be set manually, which is usually fixed as 20 ℃.

APPENDIX C – A Validation of COMSOL with the Published Work

This appendix aims to provide some validations for the COMSOL solutions with the published works. Since the sensor design is varying for different publications, the frequency responses of them are widely divergent. Therefore, the validation mainly focuses on the verifications of the Rayleigh wave velocity in certain material due to its constant property even if the device dimensions are changing.

A published Rayleigh wave velocity of 3488 m/s in a $LiNbO_3$ substrate has been raised by (Adler, 2000; Campbell, 1998) and validated by several previous works. In (Krishnamurthy, 2007), a two-port $LiNbO_3$-based SAW-DL sensor with a wavelength of 34.88 μm was developed, and its center frequency was is measured using the Agilent 4396B Spectrum/Network/Impedance Analyzer, as shown in Figure C.1.

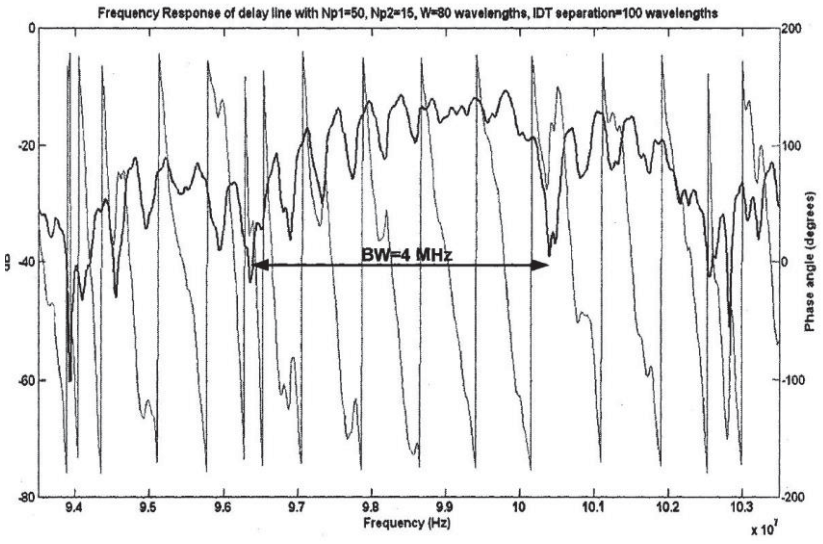

Figure C. 1 Frequency response of delay line obtained from (Krishnamurthy, 2007).

The center frequency appeared near 99 MHz; therefore, the Rayleigh wave velocity could be calculated using Equation 2.10, which is 3,453 m/s. The result was close to the 3,488

m/s with an error of 1%, which might be because of several factors such as mass loadings and experimental errors.

In (Kannan, 2006), the frequency response of a $LiNbO_3$-based SAW resonator was evaluated using ANSYS. The Rayleigh wave velocity was calculated in the same way as discussed before and analyzed in terms of some factors from the device dimensions as shown in the Table C.1,

Table C.1

Velocity and reflectivity calculated by (Kannan, 2006).

MR	***h/λ***	**Velocity (m/s)**
0.4	3.0%	3,897
0.4	3.4%	3,889
0.5	2.4%	3,894
0.5	3.0%	3,883
0.6	3.0%	3,872

where MR represents the metallized ratio, and h/λ is the finger height to wavelength ratio. It can be concluded that both of these two factors would affect the ultimate Rayleigh wave velocity, whereas these velocities are very close to the 3488 m/s.

In this thesis work, the center frequency of the designed $LiNbO_3$-based SAW sensor with a 300 μm IDT wavelength is evaluated as 11.4 MHz by using the COMSOL Multiphysics. The Rayleigh wave velocity is calculated around 3,820 m/s as analyzed in chapter 4, which is well fitted with the published results. It demonstrates that the built-in PDEs in COMSOL for solving the physical phenomena can absolutely support the real-life cases and is reliable to evaluate this thesis subjective.